JMEPEG
https://doi.org/10.1007/s11665-026-14397-7

1059-9495/$19.00

ORIGINAL RESEARCH ARTICLE

Study on the Tribological Properties of Textured Coatings Prepared by the Dual-Laser Method

Xina Wang, Na Tan, Changqing Ye, Yang Li, Shulong Ye, Jingyi Tan, Yongjuan Dai, and Yang Ding

Submitted: 13 January 2026 / Revised: 15 May 2026 / Accepted: 3 June 2026

To address severe wear-induced failures in marine equipment, a marine steel substrate was coated with a eutectic high-entropy $AlCoCrFeNi_{2.1}$ alloy in this study via laser cladding (LC). Laser surface texturing (LST) was subsequently employed to create microtextures of different shapes (circular, square, and hexagonal) to address the inherent issue of higher friction coefficients in coatings prepared via LC. The experimental results demonstrated that all textured coatings outperformed their nontextured counterparts in terms of both wear resistance and friction reduction. Microscopic characterization through testing methods such as SEM, XPS, and EBSD revealed that the cross-sectional structure of the coating was significantly refined after laser etching, the dislocation density increased significantly, and the in situ generation of Al_2O_3/Cr_2O_3 oxides led the hardness in the textured to increase by 62.4 HV area compared with that in the unetched area. Among the geometries tested, the circular texture exhibited superior performance because of its favorable stress distribution, effective wear-debris entrapment, and minimal stress concentration, with an average friction coefficient of 0.59 and a minimal wear volume of 0.009 mm^3. This study clarifies the mechanism by which laser-generated microtextures increase coating durability through controlled wear-debris management.

Keywords eutectic high-entropy $AlCoCrFeNi_{2.1}$ alloy, friction and wear, laser cladding, laser surface texture

1. Introduction

Marine equipment serves as a critical tool for national development, the conservation of marine resources, oceanographic research, and the safeguarding of maritime rights and security. Its reliability and durability directly determine the effectiveness of major strategic missions. However, marine equipment operates for long periods in extremely harsh and complex environments, leading to premature failure of key components, structural damage, functional loss, and even safety accidents (Ref 1).Therefore, employing advanced technological means to enhance the performance of critical components in marine equipment is of paramount importance for extending service life, ensuring operational safety, and reducing maintenance costs.

With the rapid advancement of technology, the requirements for the surface performance of components have become increasingly stringent, particularly in terms of functional integrity and durability. Currently, the primary methods for enhancing the performance of surface coatings involve secondary processing techniques such as laser remelting and surface strengthening after coating formation (Ref 2). Since wear primarily occurs on material surfaces, their failure initiates precisely from the loss and delamination of surface material. Therefore, strengthening critical components through surface engineering technologies has become the most economical and efficient core approach for enhancing overall performance. Surface engineering technology refers to a series of techniques that alter the surface composition, microstructure, and properties of materials through physical, chemical, or mechanical methods, thereby imparting specific mechanical, chemical, or physical characteristics not inherent to the substrate. Currently, well-established surface modification technologies include magnetron sputtering (Ref 3), physical vapor deposition (Ref 4), plasma spraying (Ref 5), and laser cladding (Ref 6). Laser cladding technology has several significant advantages: metallurgical bonding (Ref 7), resulting in high bonding strength (Ref 8), controllable heat input (Ref 9), and minimal thermal impact on the substrate (Ref 10). This technology enables the preparation of dense, uniform reinforcement coatings on metal surfaces that possess good hardness and abrasion performance. It enables the fabrication of dense, uniform, and reinforced coatings on metal surfaces with great hardness and abrasive resistance. Therefore, the core advantage of laser cladding technology lies in its versatility in material selection.

By utilizing various types of powders, such as self-fluxing alloys (Ref 11), high-entropy alloys (Ref 12), and composite materials (Ref 13), it is possible to tailor functional coatings with superior properties—including exceptional abrasion performance, decay resistance, and fatigue resistance—that are specifically designed for the matrix surface. This technology

Xina Wang, Na Tan, Yang Li, Jingyi Tan, and **Yongjuan Dai**, Tianjin Key Laboratory of High Performance Precision Forming Technology and Equipment, Tianjin University of Technology and Education, Tianjin 300222, China; **Changqing Ye** and **Shulong Ye**, National-Local Joint Engineering Laboratory of Intelligent Manufacturing Oriented Automobile Die and Mould, Tianjin University of Technology and Education, Tianjin 300222, China; and **Yang Ding**, Faculty of Materials Science, Shenzhen MSU-BIT University, Shenzhen 518172, China. Contact e-mails: tanna6786@163.com and yechangqing@smbu.edu.cn.

Published online: 29 June 2026

represents an excellent method for increasing the wear resistance of ocean steel (Ref 14). Despite its numerous advantages, which have made it a current research focus, the coatings produced by this technology exhibit certain limitations. For instance, these coatings often exhibit a high friction coefficient and poor friction-reducing and lubricating properties. During friction processes, substantial frictional forces and significant adhesive wear occur, which may conversely lead to severe tribological damage. Therefore, while laser cladding effectively increases the hardness and wear resistance performance of a surface, how to concurrently improve its friction-reducing properties must be resolved to promote its broader application in critical marine equipment components. However, the coatings prepared by laser cladding, despite having excellent hardness and wear resistance, usually have a relatively high coefficient of friction and insufficient inherent antifriction ability. Under sliding or reciprocating friction conditions, high friction and adhesive wear are prone to occur, which limits its application in precision moving parts in marine environments that require low friction and high-energy efficiency.

Tribological research reveals that surface smoothness is not the determining factor for tribological performance; instead, the predominant mechanism stems from the microstructural characteristics of the surface. Surface texturing is a good strategy for reducing wear (Ref 15-17). Engineered surface textures with controllable micromorphologies have been proved to exceptionally enable active regulation of the contact stress distribution and lubricant film dynamics (Ref 18, 19). In recent years, biomimetic design has emerged as a promising pathway for developing novel surface textures. Through in-depth research on biomimetic structures, various functional surface textures have been developed, and corresponding precision machining technologies have concurrently advanced and been refined (Ref 20-22). Numerous investigations have confirmed that surface texture treatment is a viable way to mitigate mechanical tribology behavior (Ref 23-25). Chen et al. (Ref 26) demonstrated that constructing specific microtextures on metal surfaces can significantly enhance their tribological performance. This increase in capacity is due to the triple-effect mechanism of surface textures: a reduction in the real contact area between friction pairs, effective entrapment of wear debris, and storage of lubricating media. Triangular textured patterns, as efficient and reliable specialized structures, demonstrate remarkable friction-reducing properties. Laser surface texture (LST) technology, as an advanced manufacturing technique, plays a pivotal role in enhancing tribological performance (friction and wear properties). Microdimples fabricated on the surface of CoCrFeNiMoW coatings with optimized parameters (e.g., diameter: 100 μm; area ratio: 4%) resulted in decreases in the friction coefficient and abrasion volume of 7.73 and 42.04%, respectively. The wear theory has shifted from severe abrasive–adhesive and oxidative combined wear to mild abrasive wear and oxidative wear (Ref 27). Compared with the application of a coating via microarc oxidation (MAO) alone, application of a laser-textured triangular pattern (optimal parameter: area ratio of 9.17%) to a coating prepared via MAO on an aluminum metal surface reduced the friction coefficient by 33.07%. The wear resistance of the composite coating significantly increased: The wear depth of the smooth MAO coating reached 20 μm (complete wear-through), whereas the textured MAO composite coating exhibited no wear-through phenomenon. Under optimal texture conditions, the wear depth was substantially reduced compared with that of the substrate. The surface textures act by capturing fragments to lessen the extent of three-body abrasion, and the MAO coating provides a high-hardness support layer. Their synergistic interaction contributes to the observed high efficiency in terms of friction reduction and wear resistance (Ref 28). Compared with those in the nontextured cylinder liner, in laser-processed surface microdents (optimal parameter: area share 10%), the coefficient friction decreased by 21.58%, the wear of the cylinder liner decreased by 46.19%, the wear of the paired piston ring decreased by 50.6%, and the tensile cylinder time increased by 2.8 t. Surface microtextures significantly improve the lubrication performance and reverse the abrasive damage to friction pairs by storing lubricant, capturing wear debris, and reducing the contact area, thereby achieving highly efficient antifriction and wear resistance (Ref 29).

Furthermore, the high-power tribology of a textured surface is strongly influenced by the performance of the substrate material (Ref 30). The tribological benefits of microdimple textures have been demonstrated and extensively studied in recent research (Ref 31-33). Therefore, laser surface texturing technology has proved to be a highly effective approach for friction reduction and surface strengthening of marine steel.

Surface texture-enhancing tribological properties have been extensively researched, but most studies have focused on conventional metal materials (such as steel and aluminum alloys) or traditional thermal spray coatings. Research on the application of these textures to the surface of high-entropy alloys coated by laser cladding to achieve excellent comprehensive performance is still insufficient. The selection of materials for coatings prepared by laser cladding is critical to their service performance in marine environments. Given that marine equipment operates long term under extremely complex conditions—including high salinity, high humidity, high pressure, low temperatures, and microbial adhesion—single-metal or traditional alloy systems (e.g., stainless steel and nickel-based alloys) often struggle to simultaneously meet the combined requirements for corrosion resistance, abrasion performance, and great strength. Their performance shortcomings readily lead to premature coating failure. High-entropy alloys have emerged as a multielement design concept and have overcome the limitations of traditional alloys dominated by one or two primary elements. By leveraging their unique traits, including the effects of high entropy, lattice distortion, slow diffusion, and mixing (Ref 34), high-entropy alloys are a groundbreaking material for developing a new generation of specialized protective coatings for marine equipment (Ref 35, 36). High-entropy alloys demonstrate outstanding properties such as high rigidity (Ref 37), good abrasion performance (Ref 38), and excellent high-temperature stabilizing power (Ref 39). Various fabrication techniques have been developed to synthesize HEAs, such as steel metallurgy (Ref 40), mechanical metalwork (Ref 41), hot spraying (Ref 42), and laser cladding (Ref 43). This is what traditional coating materials struggle to achieve. A comparative evaluation revealed that the pitting corrosion resistance of CoCrFeNi materials in a simulated seawater environment is markedly greater than that of 304 stainless steel (Ref 44). By introducing specific elements for optimization, the performance of coatings under harsh working conditions can be enhanced. As reported by Liu (Ref 45), the addition of Mo to the CoCrFeNiMo system successfully refined the coating microstructure. While significantly increasing the hardness, the formation of MoO_3– and (Mo, Cr)-oxidelubricated films concurrently endowed the coating with superior friction-reducing and abrasive resistance properties. Another study revealed that by modulating the aluminum content in the AlCoCrFe system, the hardness and toughness of the coating can be balanced, thereby effectively suppressing the initiation and propagation of cracks under cyclic stress and significantly extending the service life of the coating under synergistic corrosion–wear conditions (Ref 46). Bui (Ref 47) researched the scratch deformation behavior and subsurface damage of a high-entropy NiCoCrFe alloy and revealed that the maximum tangential force and average coefficient of friction of the material increased with decreasing Fe content. Conversely, increased Co content intensified wear. Application of both laser surface texturing (LST) and a diamond-like carbon (DLC) coating on a WC-Co cemented sample can achieve a 91.01% reduction in the coefficient of friction and a 95.06% reduction in the wear rate under dry friction conditions. The synergistic effect is attributed to texture-induced stress regulation and the improved chemical stability of the coating (Ref 48). In addition, the combination of bionic geometric textures (such as hexagonal, rhombic, fan-shaped, and ring-shaped sectors) and TiAlN coatings has been proved to effectively regulate the wear pattern and interfacial stress distribution of materials under different loads and frequencies, thereby decreasing the wear depth by more than 25% under extreme conditions (Ref 49). Pulsed laser surface remelting (PLSR) reduces the coefficient of friction of Ti6Al4V from 0.63 to 0.31 by inducing martensitic transformation and microscopic corrugated structures and significantly increases the corrosion resistance and biocompatibility (Ref 50). From the perspective of surface strengthening, laser shock peening (LSP) is widely used to increase the wear resistance and fatigue resistance of metal components because of its ability to introduce residual compressive stress and refine the hardened grain layer within the material (Ref 51). In addition, to satisfy the wear resistance, ice resistance, and corrosion resistance requirements, laser-induced superhydrophobic texture technology simultaneously achieves wettability, ice adhesion behavior, and wear resistance by regulating the pulse width and substrate preheating means that the EG690 marine steel substrate was placed on a heating platform and heated to 300 °C for 30 min prior to laser cladding, providing a new approach for designing lightweight metal components for outdoor use (Ref 52). Furthermore, the coupling of microtexture and thin-film coating technology also results in significant strengthening potential. Microtextures can optimize surface morphology and grain characteristics before deposition, increasing the microhardness, resistance to plastic deformation, and wear resistance of the coating by 14-36% and effectively suppressing adhesive wear (Ref 53). Therefore, on the basis of the excellent strength, toughness, and environmental tolerance of high-entropy alloys owing to their multiprincipal design, their use as a laser cladding material and application of a laser texture on their surface is expected to achieve a synergistic effect of "1 + 1 > 2" from the perspective of tribological interface regulation. This provides a novel composite surface engineering strategy for simultaneously addressing the challenges of wear resistance, corrosion resistance, and friction reduction faced by marine equipment components.

Recent studies have shown that laser surface texturing (LST) is an effective strategy for improving the tribological performance of high-entropy alloy (HEA) surfaces. Hu et al. fabricated microdimple textures on laser-cladded CoCrFeNiMoW HEA coatings and reported that optimized dimples reduced the friction coefficient and wear volume by 7.73 and 42.04%, respectively, mainly by decreasing direct contact, capturing abrasive debris, and mitigating oxidation during sliding (Ref 27). More generally, LST can tailor surface functionality through the coupled effects of geometric texture and laser-induced surface chemistry, which is particularly important for wear and corrosion-related applications (Ref 54). In corrosive or oxidative wear environments, surface textures can act as microreservoirs for wear debris and corrosion products, while friction-induced oxidation promotes the formation of compact oxide/passive tribolayers. Such oxide tribolayers have been reported to significantly reduce the friction coefficient and wear rate of laser-cladded HEA composite coatings at elevated temperatures (Ref 55). Therefore, the "texture–debris entrapment–oxidative strengthening" mechanism provides an important theoretical basis for designing laser-textured HEA coatings with enhanced tribocorrosion resistance.

In conclusion, to fill the current gap in the understanding of the tribological synergistic mechanism of "texture morphology-high-performance coatings," this study aims to systematically explore the influence of laser surface texturing on the friction and wear behavior of high-entropy alloy with laser clad coatings. Eutectic $AlCoCrFeNi_{2.1}$ high-entropy alloy coatings were fabricated on the surface of marine steel by laser cladding, and then, microdent textures of different geometric shapes (circular, square, and hexagonal) were processed on its surface by laser etching. By comparing the tribological properties of textured and nontextured coatings, the influence of texture morphology on the behavior of debris and the effect of its mechanism of action on the transformation of wear mechanisms are analyzed, with the aim of providing a theoretical and experimental basis for the design of high-performance composite surfaces for extreme marine environments.

2. Experimental

2.1 Materials and Coating Preparation

The raw sheet material used was E690 alloy, with dimensions of 120 × 120 × 85 mm. Prior to testing, the substrate surface was ground cleaned. The cladding material was $AlCoCrFeNi_{2.1}$ powder with a purity of ≥ 99%. The proportions of each element are shown in Table 1. The particle size of the powder ranged from 13 to 35 μm, and the composition of the high-entropy alloy is illustrated in Fig. 1. SEM micrographs of the powder morphology at magnifications of 1000 and 25000 are shown in Fig. 1(a) and (b), respectively, whereas the statistical histogram of the grain size distribution is shown in Fig. 1(c). Before the experiments were performed, the powder was dried in an oven at 120 °C for 2 h. The coating was fabricated using an LHHY-12600-Z laser cladding system. Synchronous powder feeding was adopted as the delivery method, with high-fineness argon used as both the protecting

Table 1 Proportions of each element

Element	Al	Co	Cr	Fe	Ni
at.%	16.39	16.39	16.39	16.40	34.43

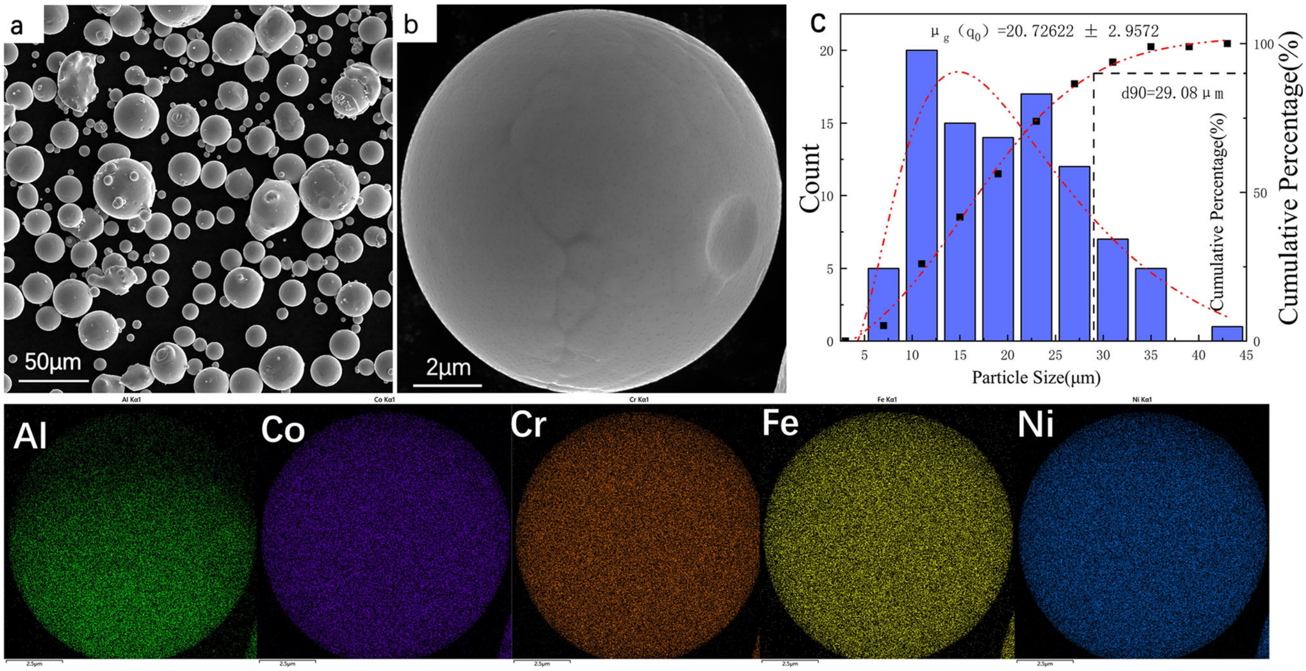

Fig. 1 SEM macromorphology of the powder: (a) SEM image at 1000 magnification, (b) SEM image at 25000 magnification, and (c) histogram of the particle size distribution for the powder

Table 2 Processing parameters of the coating

Process parameter	Value
Laser power, W	2800
Laser scanning speed, mm, s	200
Overlap, %	80
Powder delivery rate, g, at.%	20
Shielding gas flow, L, min	15
Powder delivery flow, L, min	10
Spot diameter, mm	2

gas and the carrier gas. The purity of argon is 99%. The detailed process parameters are listed in Table 2.

On the basis of preliminary experimental investigations, three types of patterns were designed, as illustrated in Fig. 2. The circular texture pattern has a diameter of 400 and a spacing of 150 μm. The square texture pattern has a side length of 400 and a spacing of 150 μm. The circumscribed circle diameter of the hexagonal texture pattern is 462, and the spacing is 150 μm. The depth of laser processing was controlled by adjusting the laser power, number of processing passes, and scanning speed. The three parameters were adjusted by assuming that higher laser power, more processing passes, and lower scanning speed collectively result in greater processing depth. The optimized parameters listed in Table 3 were ultimately determined for pattern fabrication. The surface textures were processed using an MS-M900 ultraviolet nanosecond laser marking system. The parameters are provided in Table 3.

2.2 Experimental Methods

The samples were sectioned by a wire machine for electrical release, followed by buffing and corrosion with aqua regia. The microstructure and elemental distribution of the alloy were characterized using a scanning electron microscope (ZEISS Gemini300) equipped with an energy-dispersive spectrometer. Phase analysis was conducted via x-ray photoelectron spectroscopy (Thermo Scientific ESCALAB 250Xi, USA). For electron backscatter diffraction (EBSD) analysis, $0.015 \times 0.015 \times 0.01$ m samples were prepared for electrolytic polishing, and EBSD measurements were carried out using an EDAX Hikari Plus detector integrated with a Fei Nova NanoSEM450 instrument. The Vickers hardness of the coating was measured using an HV-1000Z hardness tester under a load of 500 g and a dwell time of 15 s. Five measurements were conducted for each sample, and the average value was reported. Rectilinear reciprocating motion abrasion measurements were performed on the coatings using an MS-M900 multifunctional (electrochemical) friction tester (Huahui Instrument Co., Ltd., China) with a 6 mm alumina ball as the counterface under a normal load of 8 N and a frequency of 1 Hz for a duration of 30 min. During the friction process, the coefficient of friction was obtained. Corrosion wear was also tested using the MS-M900 multifunctional (electrochemical) friction tester (Huahui Instrument Co., Ltd., China). This instrument used a 6 mm alumina ball as the counterface, with a standard load of 8 N and a wear test time of 30 min. The three-dimensional topography of the abrasion scar was recorded using a Bruker Contour GT-K 3D optical profiler, and the wear volume was determined (Ref 56). The wear rate was calculated using Formula (1):

$$A = \frac{\Delta V}{F \times D} \quad \text{(Eq 1)}$$

A represents the wear rate, with units of mm^3/N m; ΔV is the volumetric wear amount, with units of mm^3; D is the sliding distance, with units of m; and F is the normal load, with units of N.

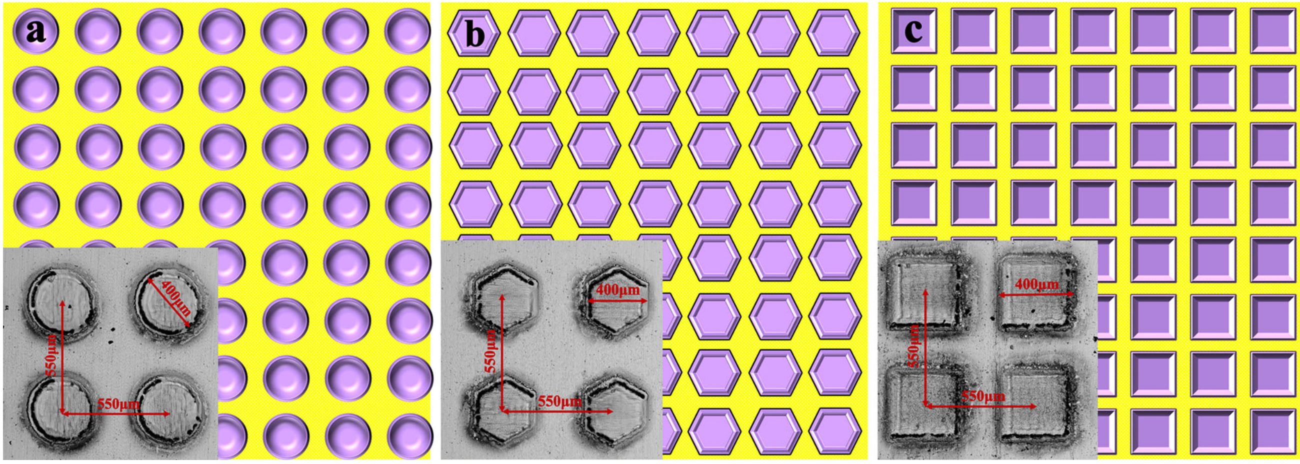

Fig. 2 Schematic diagrams of the coating microtextures: (a) $C_{C\text{-}T}$, (b) $C_{H\text{-}T}$, and (c) $C_{S\text{-}T}$

Table 3 Texture fabrication parameters

Texture Morphology	Size, μm	Texture Spacing, μm	Power, W	Number of processing passes	Scanning Speed, mm/s
Circle	200	150	800	5	500
Square	200	150	800	5	500
Hexagon	200	150	800	5	500

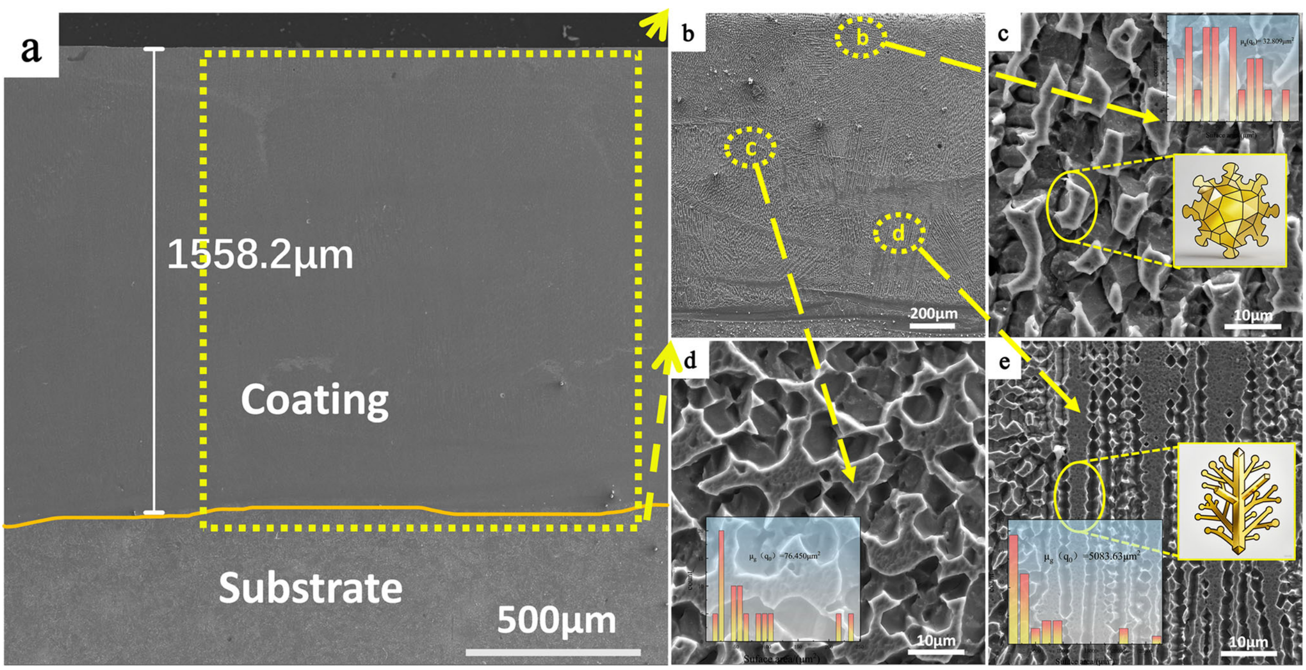

Fig. 3 SEM micrographs of the (a) $AlCoCrFeNi_{2.1}$ coating, (b) overall cross section of the coating, (c) micromorphology of the top region of the coating, (d) micromorphology of the middle region of the coating, and (e) micromorphology of the bottom region of the coating

3. Results and Discussion

3.1 Microstructural Analysis

The cross-sectional SEM image of the coating, which has a thickness of approximately 1558.2 μm, is shown in Fig. 3(a). A continuous and dense transition layer was formed at the coating–substrate interface, with no evident defects such as pores, cracks, or lack of fusion observed. These findings indicate the excellent overall integrity of the coating. Figure 3(b), (c), (d), and (e) presents magnified morphology microstructure in different areas of the coating section. Figure 3(b) displays grain morphology across the coating cross section, revealing significant variations in the grain structure from the interface to the top region. The top coating areas are due to the higher refrigeration rate and relatively fine grains; the middle region, which grows under moderate thermal conditions, consists predominantly of equiaxed grains, whereas the bottom area near the substrate, which experiences slower heat dissipation, shows a slightly increased but still uniform grain size. The microstructures of the typical regions at the top, middle, and bottom of the coating are shown in Fig. 3(c), (d), and (e), respectively. These findings further confirm the presence of a homogeneous and defect-free microstructure in each region, with the grain morphology and distribution being consistent with the typical characteristics of rapid solidification during laser cladding. This continuous, dense, and defect-free microstructure provides a robust foundation for subsequent surface texturing processes, thereby contributing to increased texturing quality and wear resistance.

Three types of textured patterns—circular, hexagonal, and square—were made on the surface of the $AlCoCrFeNi_{2.1}$ coating using a laser marking system. The SEM-derived morphologies, three-dimensional topographies, and corresponding depths of the three different patterns are shown in Fig. 4. The same laser processing parameters were applied to ensure a consistent depth across all three patterns, with each dimple region processed five times. The textured surfaces obtained through the adjustment of laser parameters are shown in Fig. 4(d), (e), and (f) and exhibit a consistent dimple depth H of 400 μm.

The scanning morphology and elemental distribution results of the coatings with different texture shapes after laser texturing are shown in Fig. 5. Aggregation of aluminum, oxygen, and a small amount of chromium can be observed on the coating surface. This aggregation is due primarily to the extreme thermochemical process induced by laser–material interactions. The high-energy laser beam results in instantaneous melting and even vaporization of the material in the irradiated zone, and the generated heat is conducted to the surrounding areas, leading to a sharp temperature rise near the etched grooves. Under high-temperature conditions, the coating material undergoes a thermal oxidation reaction, resulting in the formation of hard ceramic phases such as alumina and chromia in situ. Additionally, molten material droplets containing aluminum and chromium that ejected during the laser process are further oxidized during flight and deposition and ultimately solidify around the etched morphologies to form residues composed predominantly of these oxides.

Observe Fig. 6, to further investigate the oxidized areas, a systematic characterization of the chemical composition and microstructure of the laser-textured surface of the coating was conducted using x-ray photoelectron spectroscopy combined

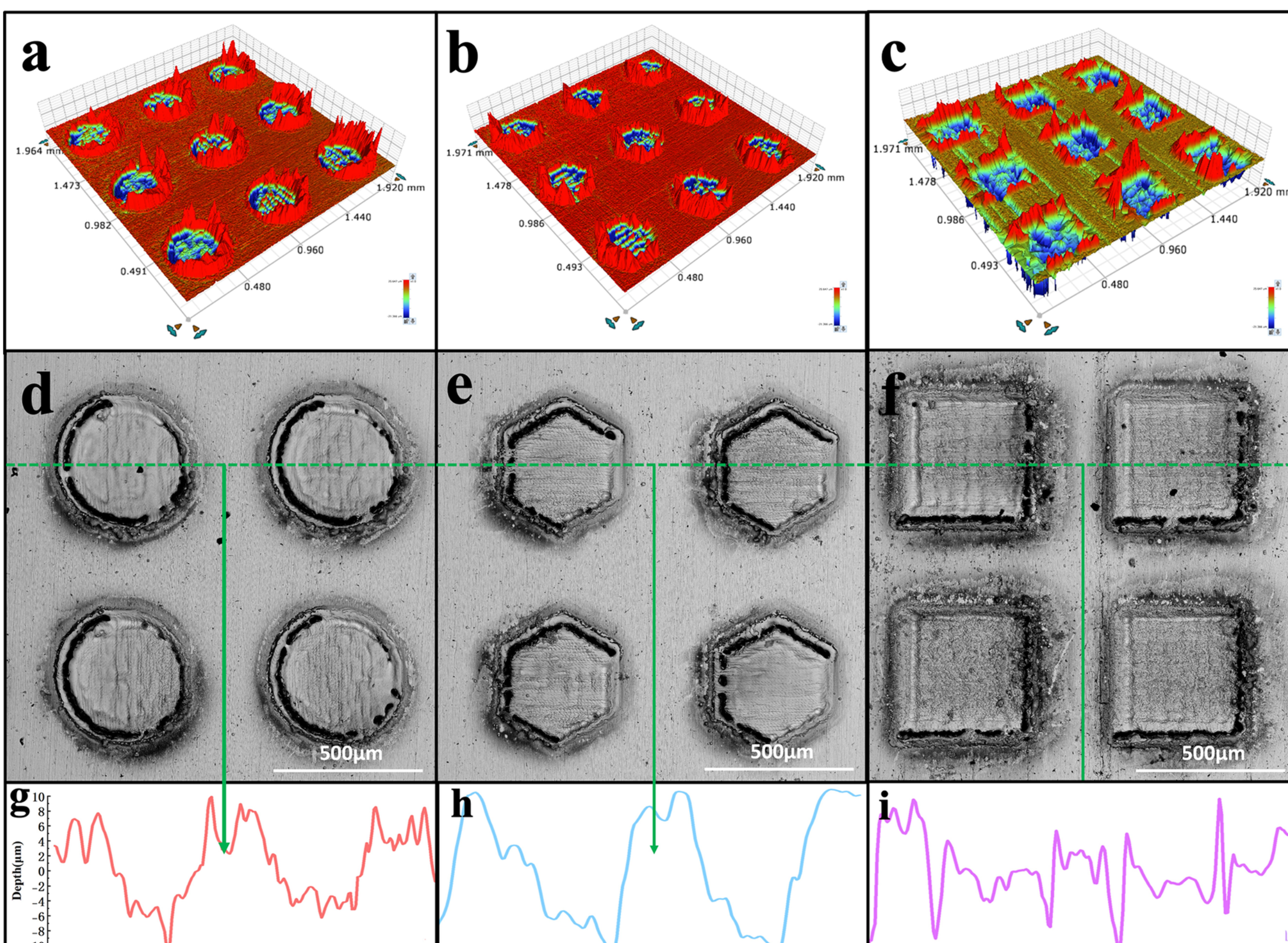

Fig. 4 Morphology of the textured patterns: (a) $C_{C\text{-}T}$ 3D morphology, (b) $C_{H\text{-}T}$ 3D morphology, (c) $C_{S\text{-}T}$ 3D morphology, (d) $C_{C\text{-}T}$ SEM-derived morphology, (e) $C_{H\text{-}T}$ SEM-derived morphology, (f) $C_{S\text{-}T}$ SEM-derived morphology, (g) $C_{C\text{-}T}$ cross-sectional profile, (h) $C_{H\text{-}T}$ cross-sectional profile, and (i) $C_{S\text{-}T}$ cross-sectional profile

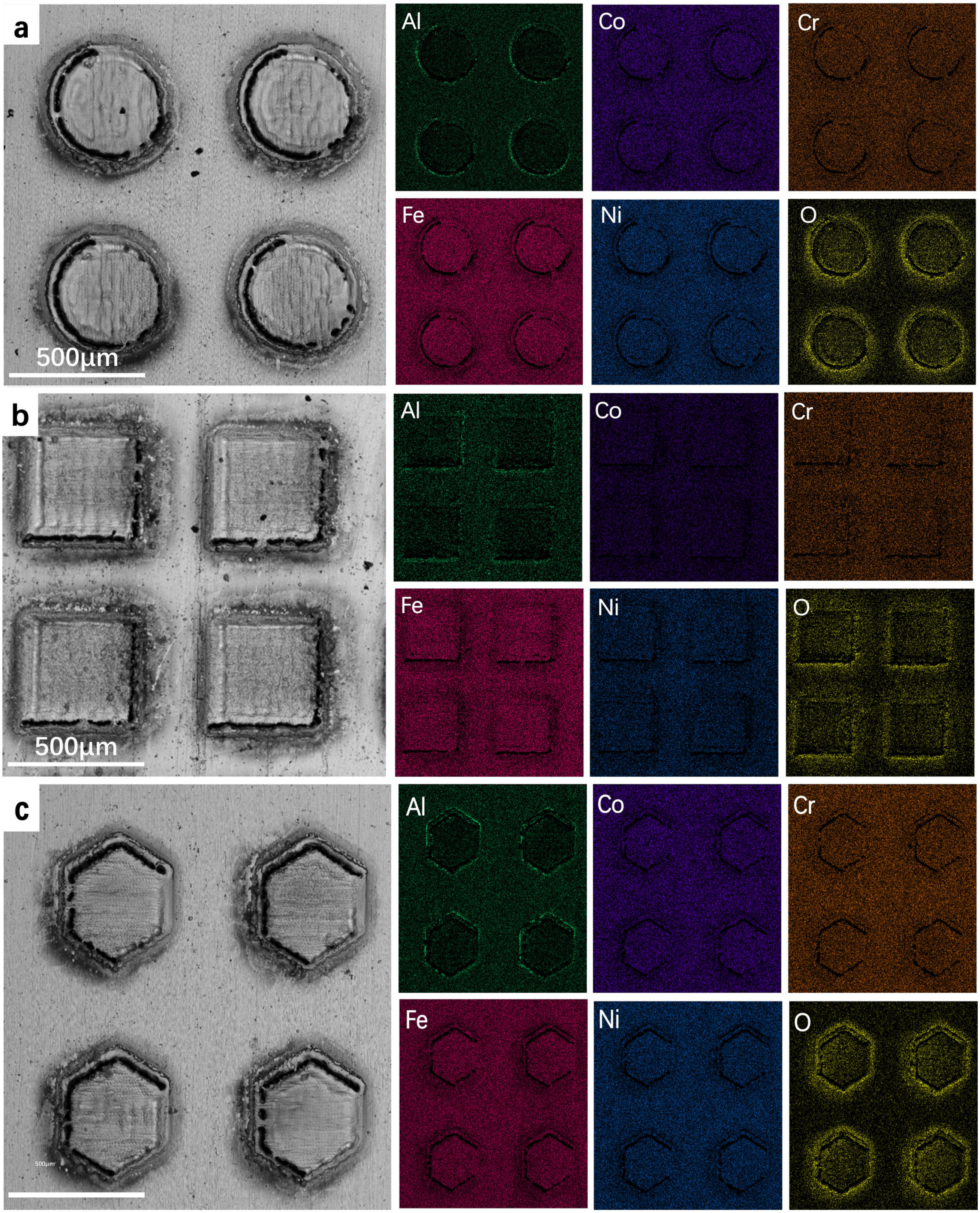

Fig. 5 SEM images and EDS results of different textured patterns applied to the $AlCoCrFeNi_{2.1}$ coating: (a) $C_{C\text{-}T}$, (b) $C_{S\text{-}T}$, and (c) $C_{H\text{-}T}$

with scanning electron microscopy and energy-dispersive x-ray spectroscopy. The consistent results from these analyses confirmed that a significant oxidation reaction occurred after texturing, with Al_2O_3 and Cr_2O_3 identified as the primary products. In the high-resolution XPS spectra, the characteristic peaks of Al at 74.3 eV and Cr 2p at 576.8 eV confirm the presence of Al-O and Cr-O bonds, respectively, which align well with the standard binding energies of Al_2O_3 and Cr_2O_3.

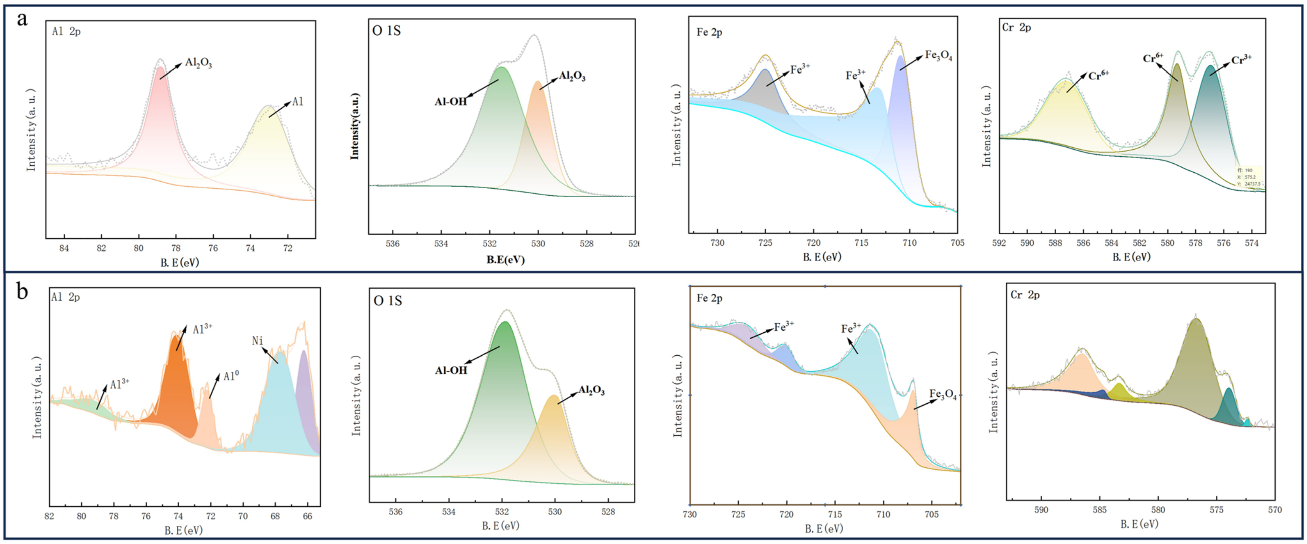

Fig. 6 (a) X-ray diffraction (XRD) pattern of the $AlCoCrFeNi_{2.1}$ coating and (b) XRD pattern of the $AlCoCrFeNi_{2.1}$ coating after etching

The SEM images reveal that the textured surface is covered by a continuous and dense reaction layer, exhibiting a morphology distinct from that of the untreated regions. EDS elemental mapping and point analysis further indicate significant oxygen enrichment within the etched zones, with the spatial distributions of aluminum and chromium being highly correlated with that of oxygen. These findings confirm the formation of Al_2O_3 and Cr_2O_3 oxides from an elemental distribution perspective. The conclusions of the multiple characterization methods corroborated with each other, indicating that the in situ oxidation behavior induced by laser texturing effectively strengthened the coating surface.

The EBSD results for the magnified areas of the coating cross section before and after laser treatment are shown in Fig. 7. The IPF images of the coating before and after laser treatment are shown in Fig. 7(b1) and (b2), respectively, and significant differences in the grain structure can be observed. Prior to etching (Fig. 7b1), the coating exhibited relatively large grain sizes and elongated or columnar morphologies, indicating a distinct directional distribution and significant preferred orientation. As shown in the grain size statistics in Fig. 7(c1), large grains within the size range of 300-450 μm accounted for up to 65% of the microstructure. This coarse-grained structure originated from the laser cladding process, where slow solidification and intense thermal gradients triggered a preferred growth mechanism—specifically, the epitaxial growth of columnar crystals induced by the direction of heat flow. This behavior aligns with the principles of dendritic coarsening and preferential growth during the solidification of high-entropy alloy melt pools (Ref 57). In contrast, after surface texturing (Fig. 7b2), the grains were significantly refined, the microstructure became more equiaxed and densely distributed, and the random orientation was notably enhanced. The grain size statistics in Fig. 7(c2) indicate that the grains were predominantly concentrated in the range of 50-150 μm, indicating that grain refinement in the coating was induced by remelting and rapid solidification. This phenomenon is primarily attributed to the extreme thermal gradients and melt pool turbulence caused by the secondary heat input during laser texturing. These conditions resulted in partial remelting and mechanical fragmentation of the original dendrites, promoting the formation of new nuclei and inhibiting preferential grain growth. Consequently, many nonpreferred grains underwent simultaneous nucleation and rapid growth, ultimately forming a fine, equiaxed, and randomly oriented microstructure.

The KAM maps (Fig. 7d1 and d2) and their corresponding statistical histograms (Fig. 7e1 and e2) provide further evidence for the dislocation activities underlying the microstructural evolution. The kernel average misorientation (KAM) values of the coating prior to surface texturing were generally low, with an average value of 0.37. The predominant deep blue color in the image indicates small local orientation differences within the grains, a low degree of plastic strain, and a limited dislocation density. In contrast, the KAM map of the coating after surface texturing (Fig. 7d2) exhibits a notable increase in the size of green-colored regions. Concurrently, the corresponding histogram (Fig. 7e2) reveals a rightward shift in the distribution of KAM values, with the average value increasing to 0.57, indicating a significant increase in the dislocation density.

Analysis of the pole and inverse pole figure (Fig. 7f1/g1 and f2/g2) further validated the evolutionary characteristics of the microstructure. The pole figure (Fig. 7f1) prior to surface treatment revealed a pronounced concentration of {001} and {111} crystallographic planes along specific orientations. Similarly, the inverse pole figure (Fig. 7g1) exhibited noticeable clustering of grain orientation points along the $<001>$ and $<111>$ directions, indicating a preferential crystallographic texture. This suggests that a strongly preferred orientation formed under the influence of thermal gradients and directional solidification mechanisms during processing. In contrast, Figure 7(f2) sample after surface treatment demonstrates a uniform dispersed intensity distribution, whereas the inverse pole figure (Fig. 7g2) shows considerably scattered grain orientations with no pronounced preferred orientation. This finding indicates that the processing treatment promoted the randomization of the crystallographic orientation distribution, thereby significantly weakening the initial strong texture characteristics.

A combined analysis of the KAM and IPF maps revealed that the secondary thermal input introduced during the etching process not only induced grain refinement and texture weak-

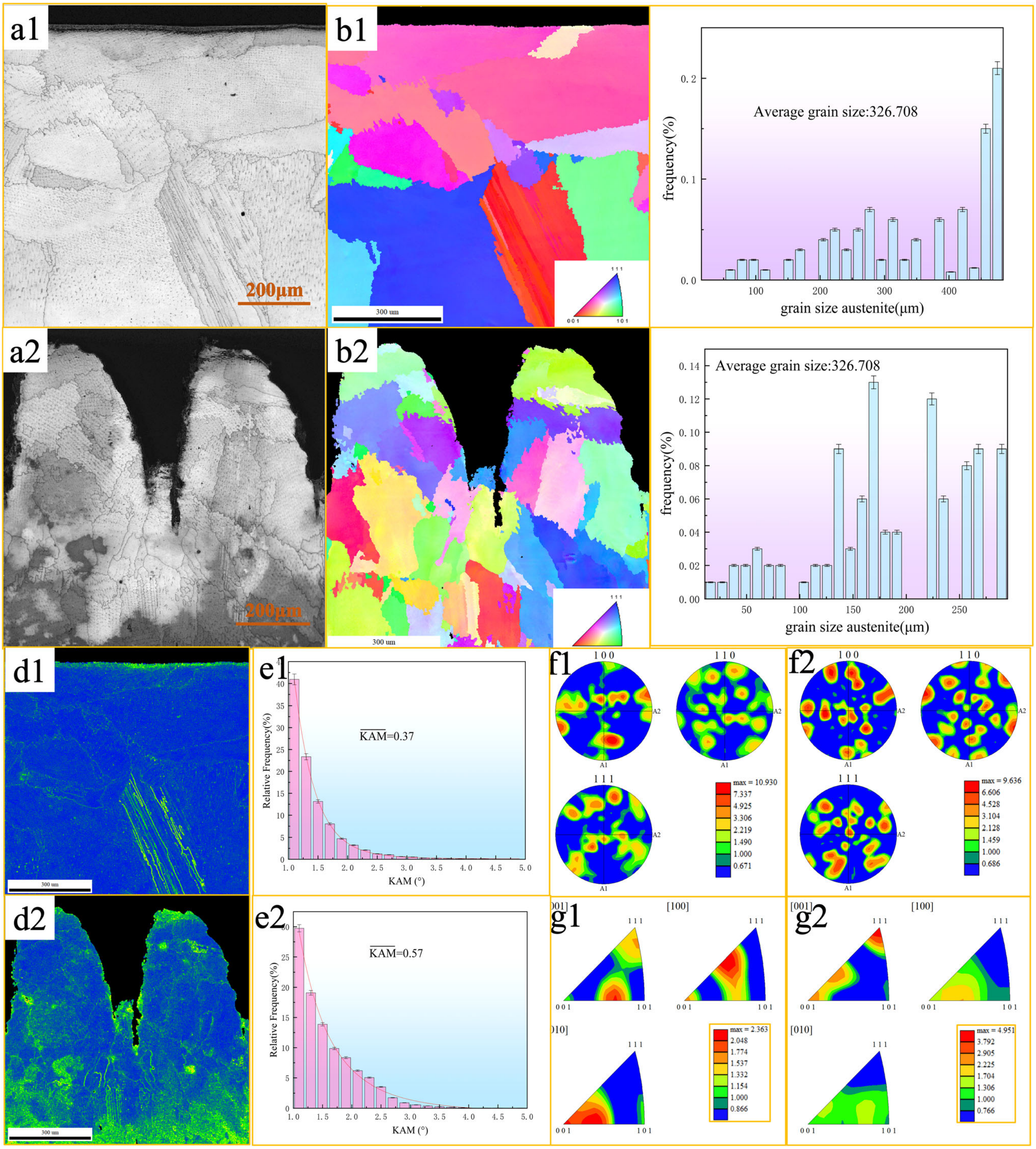

Fig. 7 EBSD characterization of the $AlCoCrFeNi_{2.1}$ coating before and after laser etching: (a) Cross-sectional morphology of the coating before and after etching, (b) grain orientation before and after etching, (c) grain size distribution before and after etching, (d) kernel average misorientation (KAM) map before and after etching, (e) KAM values before and after etching, (f) pole figure (PF) before and after etching, and (g) inverse pole figure (IPF) before and after etching

ening but also triggered dislocation multiplication through rapid solidification and microstructural reorganization, as manifested by a pronounced increase in KAM values. This indicates that the material surface underwent a significant strengthening process, where dislocation activity and microstructural rearrangement acted synergistically to form a surface-strengthened structure characterized by refined grains and a high dislocation density.

The grain refinement and increased dislocation density after laser texturing are closely related not only to laser-induced remelting and rapid solidification, but also to the intrinsic thermodynamic and kinetic characteristics of the $AlCoCrFeNi_{2.1}$ high-entropy alloy coating. During laser texturing, the localized secondary heat input produces a small molten pool with a steep thermal gradient and a high cooling rate, resulting in a large degree of undercooling. This promotes the formation of numerous nuclei during solidification, thereby contributing to grain refinement (Ref 58).

For the $AlCoCrFeNi_{2.1}$ coating with a single FCC solid-solution structure, the high configurational entropy enhances the thermodynamic stability of the FCC phase during rapid solidification. This high-entropy stabilization effect helps maintain the phase stability of the coating under rapid thermal cycling and favors the formation of a refined solidification structure. Meanwhile, the sluggish diffusion effect, which originates from the complex multicomponent atomic environment and severe lattice distortion, restricts long-range atomic diffusion during the extremely short laser–material interaction time. Consequently, grain growth and solute redistribution after nucleation are effectively suppressed, leading to a finer microstructure (Ref 59).

In addition, the rapid heating and cooling process during laser texturing generates considerable thermal stress, which promotes dislocation multiplication within the FCC matrix (Ref 60). At the same time, sluggish diffusion and lattice distortion inhibit dislocation recovery and annihilation, resulting in a higher retained dislocation density. Therefore, the microstructural evolution of the laser-textured $AlCoCrFeNi_{2.1}$ coating is governed by the combined effects of localized laser thermal input, high-entropy stabilization, sluggish diffusion, lattice distortion, and the stability of the single FCC solid-solution structure, rather than being a general rapid-solidification phenomenon applicable to all alloy coatings.

3.2 Coating Performance

After surface laser texturing, significant discrepancies in the microhardness were observed between the processed regions and the original unprocessed regions of the coating surface. As illustrated in Fig. 8, the microhardness values of the untreated regions were 307, 313, and 302 HV, with an average of 307.3 ± 5.5 HV. The relatively concentrated data distribution reflects the uniformity of the coating in its initial state. In stark contrast, the microhardness of the laser-textured regions significantly increased, reaching 358, 379, and 372 HV, with the average value increasing substantially to 369.7 ± 10.5 HV. The high numerical consistency of this strengthening effect indicates that the increase in hardness induced by laser treatment is both pervasive and effective. This increase in hardness is attributed primarily to the rapid melting and solidification effect triggered by the high-energy-density laser beam during the texturing process. Laser irradiation causes instantaneous local melting of the coating surface, followed by rapid solidification. This nonequilibrium process leads to significant refinement of the micrograins, which is a key mechanism for increasing material strength. Additionally, the rapid cooling process introduces a high dislocation density, further contributing to material reinforcement. These factors synergistically enhance the performance of the laser-treated regions. The overall upward trend of the data strongly confirms that laser surface texturing is a reliable modification technique capable of effectively increasing the surface hardness of coatings.

The average friction coefficient is 0.717 for C, 0.59 for C_{C-T}, 0.645 for C_{H-T}, and 0.662 for C_{S-T}, as shown in Fig. 9. The friction coefficient of C_{C-T} decreased by 17.71% compared with C. Compared with the nontextured coating, the textured coatings all exhibit a lower coefficient of friction, suggesting that surface texturing contributes to reducing friction.

To investigate the influence of surface coating properties, the three-dimensional morphology of the wear tracks was analyzed for each sample, as shown in Fig. 10. Comparative analysis of the morphologies in regions *a*, *b*, *c*, and *d* clearly reveals that after the tribological test, the wear debris generated on the textured coating surface accumulated predominantly around the surface dimples (Fig. 10b, c, and d). In contrast, wear debris was evenly distributed along the center and sides of the abrasion trajectory on the nontextured coating (Fig. 10a). The magnified images of regions a2 to d2 further demonstrate that the dimple textures act as physical reservoirs, effectively trapping wear debris and thereby preventing it from entering the friction interface and inducing abrasive wear. However, it should also be noted that a considerable amount of debris remains on the wear track of the textured surfaces, particularly in the central regions, indicating that surface textures do not

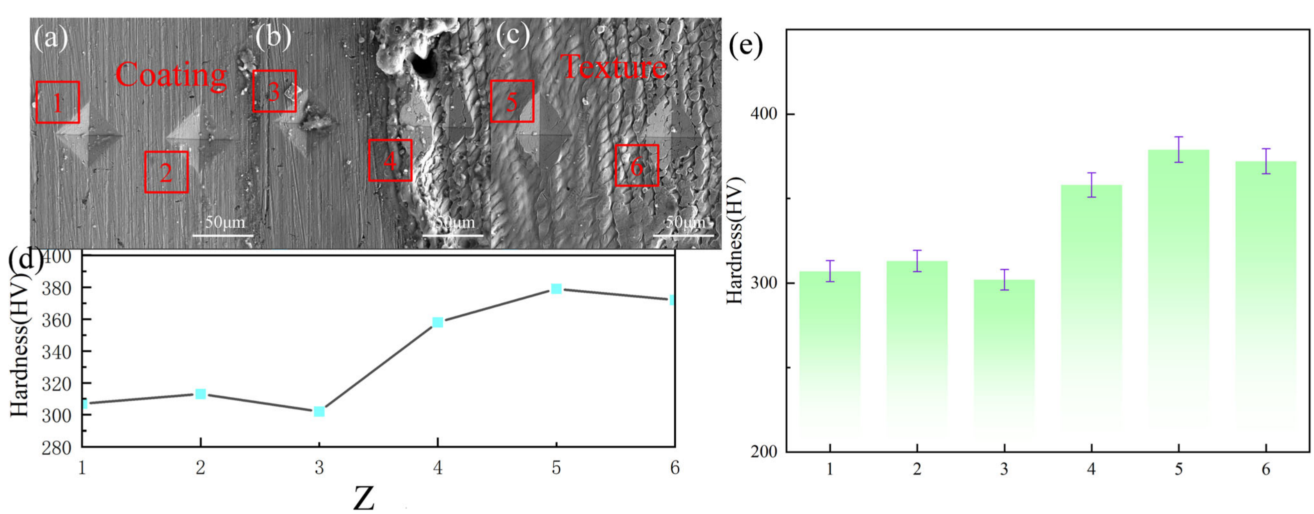

Fig. 8 Hardness analysis: (a) SEM morphology; (b) hardness distribution map; (c) average hardness; (d) hardness distribution map; and (e) regional average hardness

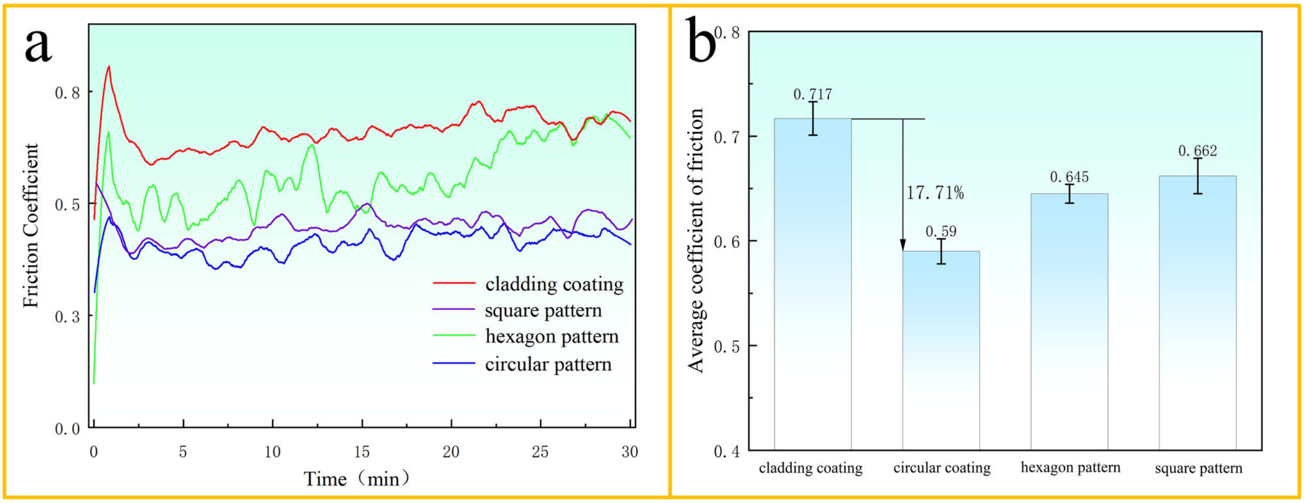

Fig. 9 Tribological properties of the $AlCoCrFeNi_{2.1}$ coating and coatings with different etched textures: (a) dynamic curves of the average friction coefficient and (b) histogram of the average friction coefficient

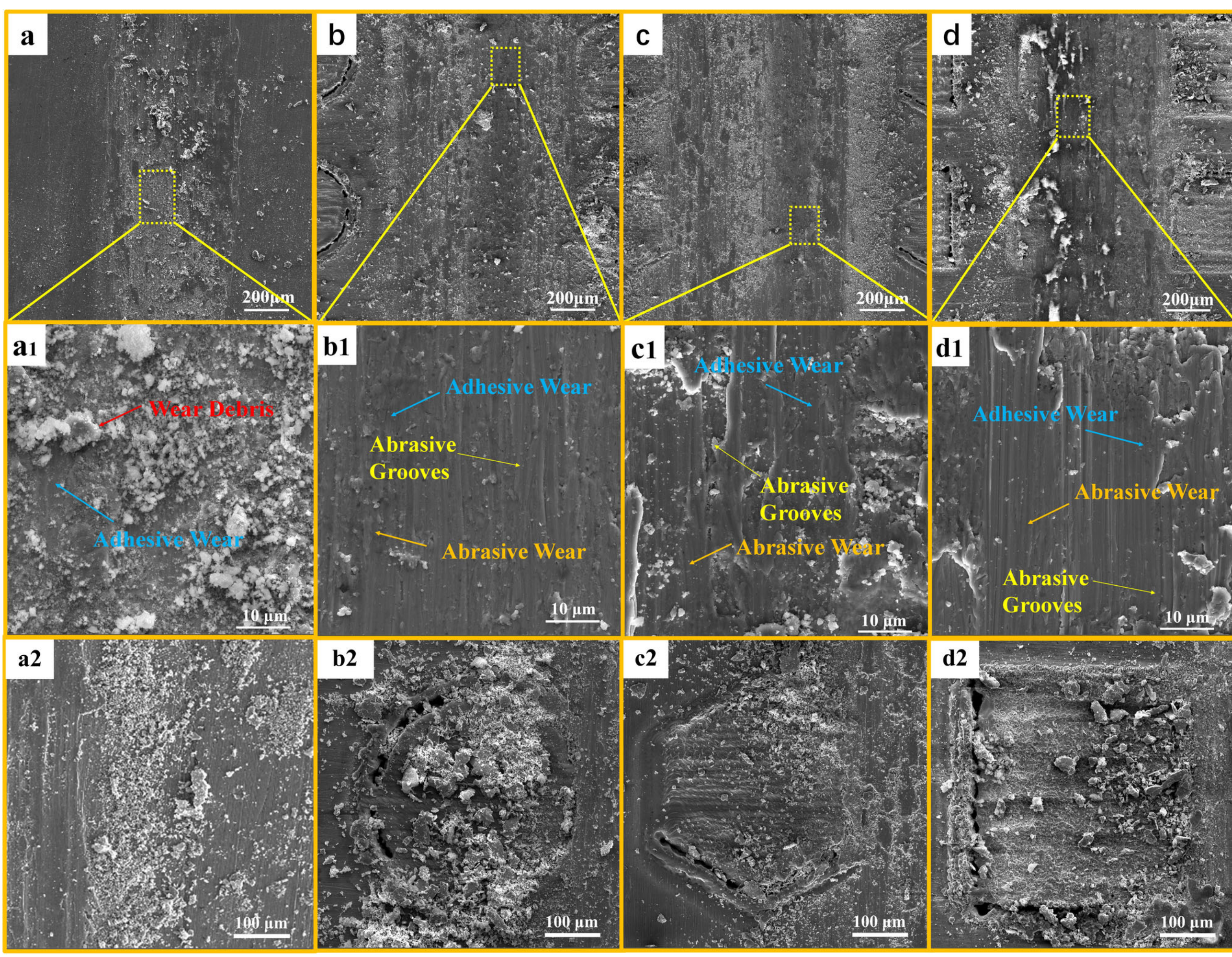

Fig. 10 SEM micrographs of the wear-scar morphology on the coating surface: (a) C, (b) $C_{C\text{-}T}$, (c) $C_{H\text{-}T}$, and (d) $C_{S\text{-}T}$

eliminate debris accumulation but rather modify its spatial distribution.

At a magnification of 5000 ×, the wear track of coating C (Fig. 10a1) exhibited characteristics of both abrasive wear and adhesive wear, whereas the textured coatings (Fig. 10b1, c1, and d1) exhibited primarily adhesive wear. This phenomenon is closely related to the tribological characteristics under dry sliding conditions: Owing to the absence of a lubricant isolating layer, direct contact between the friction pairs occurs, resulting in extremely high localized pressure. The frictional heat generated increases the temperature in the contact zone, which induces material softening, promotes plastic deformation and interatomic diffusion, and ultimately leads to adhesive wear. Although debris is still present on the textured surfaces, most of the free-cutting particles that would typically contribute to three-body abrasion are effectively captured within the dimples or compacted into relatively stable layers within the wear track, reducing their ability to reenter the friction interface. Moreover, under normal circumstances, adhesive wear usually causes more severe material interface damage than abrasive wear.

Therefore, the improvement in wear performance is due to the reduction in the number of active abrasive particles involved in repeated cutting actions. Although such adhesive wear is difficult to completely avoid under dry sliding conditions, this adverse effect is significantly compensated for by the ability of surface textures to capture abrasion particles, which effectively suppresses abrasive wear. Therefore, the improvement in wear performance is due to the reduction in the number of active abrasive particles involved in repeated cutting actions.

Regions a2 to d2 illustrate the distribution of wear debris within surface dimples of different geometries(C-T, S-T, and H-T) under identical experimental conditions. The $C_{C\text{-}T}$ dimples captured a significantly larger amount of wear debris than the $C_{H\text{-}T}$ and $C_{S\text{-}T}$ dimples did. The $C_{C\text{-}T}$ dimples were almost completely filled with wear debris. In contrast, the $C_{H\text{-}T}$ and $C_{S\text{-}T}$ dimples were only partially filled, with wear debris being concentrated primarily at the bottom or along the edges in the sliding direction. Their debris filling ratios were significantly lower than those of the $C_{C\text{-}T}$ dimples. This finding is attributed primarily to differences in flow characteristics resulting from the distinct geometric shapes. Circular dimples feature continuous and smooth curved walls with no flow-dead zones, which promotes efficient debris containment. Once it enters the dimples, the wear debris tends to follow vortex-like flow patterns within the pit, making it difficult to escape. This results in highly efficient capture, a uniform distribution inside the dimple, and, ultimately, a high filling rate. In contrast, square and hexagonal dimples exhibit pronounced sharp corners, such as the four internal angles in square dimples. These sharp corners induce flow separation and vortex stagnation, creating "flow-dead zones." Although wear debris may be carried into the dimples, it tends to move along the flat walls rather than entering the sharp corner regions. As a result, the debris is more likely to be carried out after brief retention in the central or main flow zone of the dimple, rather than being stably captured in dead zones, leading to reduced overall capture efficiency.

EDS mapping analysis of the wear scar at 500 × magnification (Fig. 11) indicates that the textured regions of the scar exhibit a higher oxygen content than the nontextured regions do. Under dry sliding conditions, the circular surface texture results in a stable composition and uniform oxide coating at the friction interface owing to its unique geometric morphology. These oxides act as barriers that prevent friction pairs from immediately touching the solid lubricant. This effect decreases the friction coefficient, resulting in excellent antifriction and antiwear properties. The hexagonal surface texture had the highest oxygen content within its wear track, indicating that a more intense oxidation reaction occurred in this region, resulting in the generation of a substantial amount of oxidation products. However, these oxides are loosely structured and weakly bonded, making them highly prone to spallation during the wear test, thus generating abrasive debris. The dislodged debris enters the friction contact interface and participates in three-body wear, thereby significantly increasing the friction coefficient and adversely affecting the tribological performance.

The relatively high oxygen content detected on the hexagonal textured surface indicates the occurrence of oxidative wear. However, this does not necessarily imply the formation of a stable protective oxide film. Under repeated contact stress and shear during sliding, the surface oxide layer may crack and become susceptible to spallation. The detached oxide debris can then act as third-body particles and accelerate local material removal. Moreover, adhesive wear usually causes more severe interfacial damage than abrasive wear due to repeated adhesion and tearing at the contact interface. Therefore, the wear behavior of the hexagonal texture is mainly attributed to the combined effects of adhesive wear and oxidative wear, accompanied by potential oxide-layer cracking and detachment.

The 3D topography of the wear-scar depths for the various coatings is shown in Fig. 12. The textured coatings clearly exhibit shallower scars than the nontextured coating does. Quantitative analysis revealed that the damage volume was 0.024 for coating C, 0.009 for $C_{C\text{-}T}$, 0.011 for $C_{H\text{-}T}$, and 0.013 mm^3 for $C_{S\text{-}T}$. Furthermore, the wear depth profiles in Fig. 11(f) reveal the following order of scar depth: C > $C_{S\text{-}T}$ > $C_{H\text{-}T}$ > $C_{C\text{-}T}$. In terms of contact geometry, the $C_{C\text{-}T}$ texture exhibits point contacts, forming microscopic circular interfaces that, together with the nontextured regions, create a functionally discrete composite contact zone. This configuration promotes a uniform stress distribution, resists crack initiation, and generates a continuous and symmetrical hydrodynamic pressure effect. In contrast, the $C_{S\text{-}T}$ and $C_{H\text{-}T}$ textures exhibit either point contacts (at corners) or line contacts (along edges), resulting in complex microscopic contact geometries. Their sharp corners and edges tend to cause stress concentration, and although they also form composite contacts with the flat areas, these geometric features act as intrinsic stress concentrators that readily initiate fatigue cracks. This leads to microcrack propagation and accelerated material spallation. The dislodged hard debris subsequently acts as third-body abrasives, inducing severe fluctuations in friction. Localized high pressure also promotes adhesive wear and plastic deformation, generating a higher friction coefficient and the greatest damage volume among the tested coatings. On the basis of this comparison, the wear resistance of $C_{C\text{-}T}$ is superior to that of $C_{S\text{-}T}$ and $C_{H\text{-}T}$. This is attributed primarily to its favorable stress distribution characteristics: The absence of sharp corners in the $C_{C\text{-}T}$ design prevents localized stress concentration, effectively inhibiting the initiation and propagation of microcracks and thereby delaying the progression of fatigue wear. The sharp corners in polygonal textures (such as those of $C_{S\text{-}T}$ and $C_{H\text{-}T}$) readily act as stress concentration points, accelerating material damage spallation. Furthermore, the uniform stress distribution from touching and geometrically defect-free morphology of $C_{C\text{-}T}$ contributes to increased durability under cyclic loading. In contrast, the high stress concentrated at the corners of the polygonal textures significantly increases the risk of crack initiation, thereby reducing the overall service life of the coating. In summary, owing to its uniform stress field and symmetrical hydrodynamic lubrication behavior, $C_{C\text{-}T}$ demonstrates superior overall performance in terms of reducing wear, suppressing crack propagation, and extending the service life of

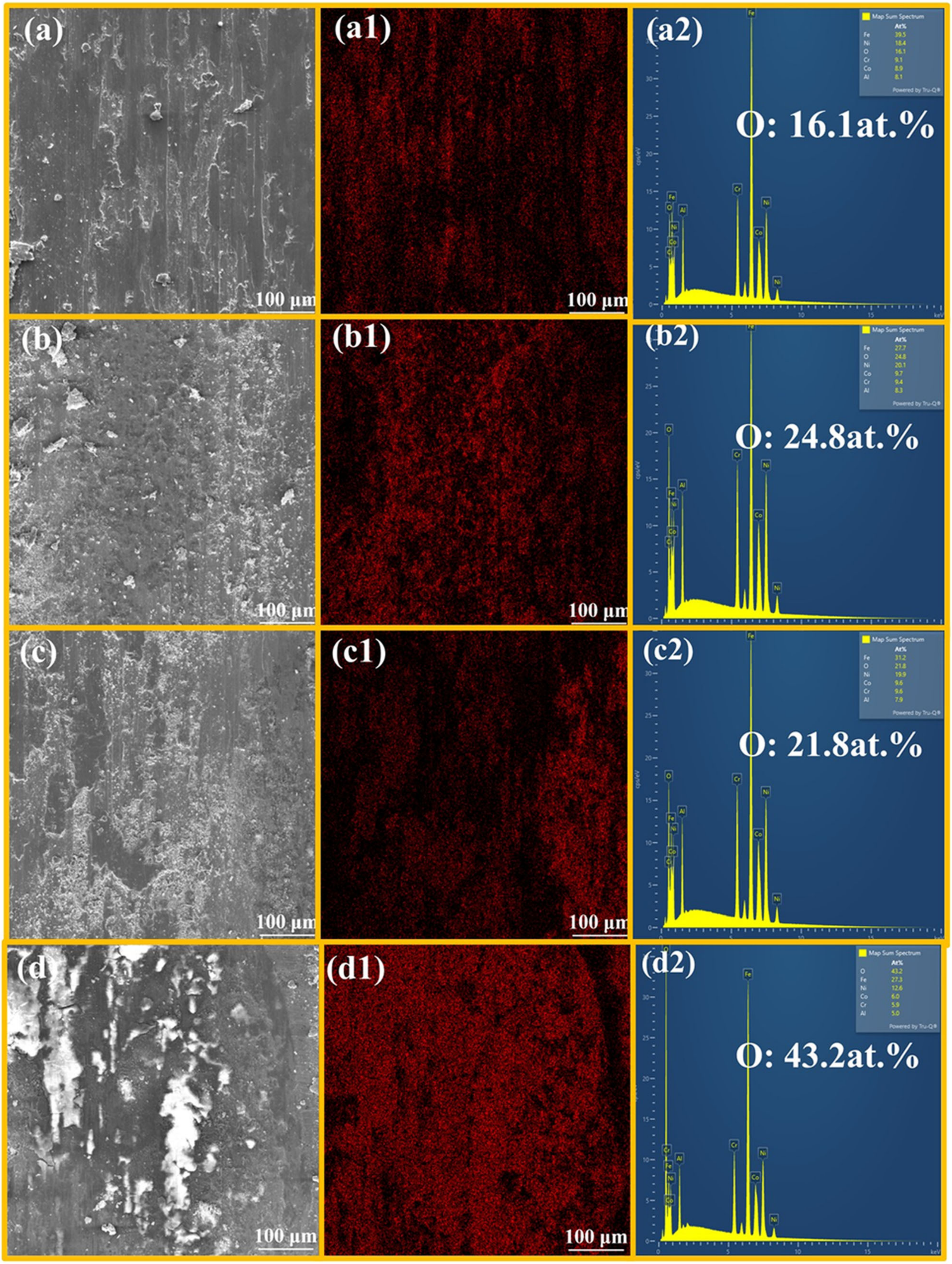

Fig. 11 SEM morphology of the wear tracks of (a) C, (b) $C_{C\text{-}T}$, (c) $C_{H\text{-}T}$, (d) $C_{S\text{-}T}$; corresponding oxygen distribution maps of (a1) C, (b1) $C_{C\text{-}T}$, (c1) $C_{H\text{-}T}$, (d1) $C_{S\text{-}T}$; and quantitative oxygen content of (a2) C, (b2) $C_{C\text{-}T}$, (c2) $C_{H\text{-}T}$, (d2) $C_{S\text{-}T}$

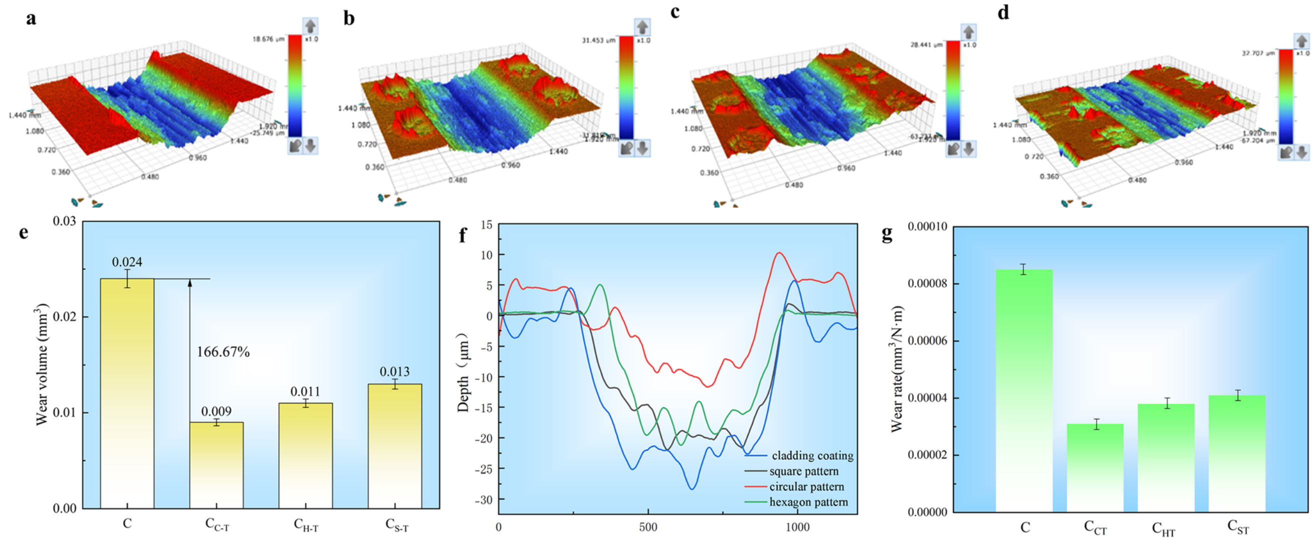

Fig. 12 Tribological properties of the coating: (a–d) 3D morphology after wear; (e) average wear volume; (f) cross-sectional profiles of the worn surfaces; and (g) wear rate

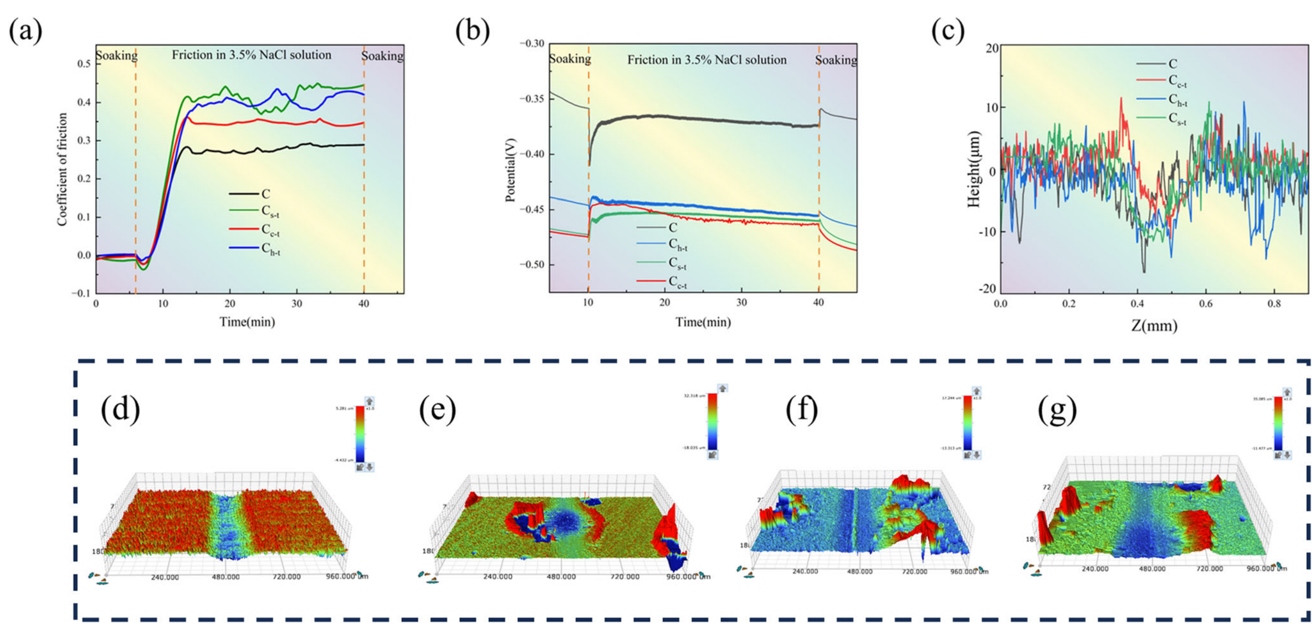

Fig. 13 White-light interferometry analysis of tribocorrosion behavior: (a) tribocorrosion potential curve; (b) tribocorrosion friction coefficient curve; (c) two-dimensional profile of the tribocorrosion wear track; (d) white-light morphology of the tribocorrosion wear track on the C coating; (e) white-light morphology of the tribocorrosion wear track on C_{C-T}; (f) white-light morphology of the tribocorrosion wear track on C_{S-T}; and (g) white-light morphology of the tribocorrosion wear track on C_{H-T}

the coating, thereby outperforming both C_{S-T} and C_{H-T} in terms of wear resistance. As shown in Fig. 12(g), the wear rate is 0.000085 for C, 0.000031 for C_{C-T}, 0.000038 for C_{H-T}, and 0.000041 mm^3/N m C_{S-T}. The calculated wear rates of the C, C_{C-T}, C_{H-T}, and C_{S-T} coatings were 8.5×10^{-5}, 3.1×10^{-5}, 3.8×10^{-5}, and 4.1×10^{-5}, respectively. The wear rate of C_{C-T} has decreased by 63.53 compared to C. C_{C-T} has approximately 63.5% less wear volume compared to C. Among them, C_{C-T} exhibited the lowest wear rate, indicating the most effective reduction in material loss, followed by C_{H-T} and C_{S-T}, whereas the untextured C coating showed the highest wear rate. This result further confirms that surface texturing can significantly improve the wear resistance of the coating, with the circular texture providing the most pronounced protective effect. The texture clearly increases the wear resistance of the coating.

Figure 13 presents the comparative results of the friction coefficient, open-circuit potential, and wear profiles obtained from the tribocorrosion tests. During the initial immersion stage, the open-circuit potential of C stabilized at approximately − 0.35 V, whereas the initial potentials of all textured coatings were lower than that of C, with C_{H-T} at approximately − 0.45 V and C_{C-T} and C_{S-T} at approximately − 0.47 V. This is mainly attributed to the increased contact area between the material and the corrosive medium induced by the textured structures, as well as the geometric discontinuities at the texture edges, which provide corrosion-active sites. After entering the friction stage, the open-circuit potential of C decreased markedly, indicating that the passive film on its surface was disrupted and not repaired in a timely manner. In contrast, the open-circuit potentials of all textured coatings exhibited a pronounced positive shift, reflecting an active dynamic repassivation process on their surfaces. Among them, $C_{C\text{-}T}$, owing to its smooth and continuous geometry, can more uniformly distribute stress and efficiently capture and accommodate wear debris, forming stable "corrosion–wear debris" microregions within the pits and thereby enabling a more sustained repassivation process. In contrast, $C_{H\text{-}T}$ and $C_{S\text{-}T}$ exhibit weaker debris-retention capability due to the presence of corners and flow-dead zones, resulting in lower passivation ability than $C_{C\text{-}T}$.

As observed from the friction coefficient curves in (Fig. 13b), under NaCl solution lubrication, all textured coatings exhibited higher friction coefficients than C. This is because the relatively smooth surface and larger contact area of C under aqueous lubrication facilitate the formation of a stable and continuous lubricating film, thereby effectively isolating direct contact between the friction pairs. Among all the friction curves, $C_{C\text{-}T}$ exhibited the most stable friction coefficient, because the circular geometry avoided stress concentration at the corners of polygonal textures, effectively suppressing microcrack initiation and localized material spallation while ensuring a uniform distribution of contact stress. Figure 13(c) presents the wear profile curves of the coatings. It can be observed that $C_{C\text{-}T}$ exhibits the shallowest and flattest wear profile, followed by progressively deeper profiles for the $C_{H\text{-}T}$ and $C_{S\text{-}T}$ coatings, whereas C shows the widest and deepest wear profile. This result is consistent with the aforementioned mechanism, indicating that the circular texture delivers the best corrosion–wear resistance among the three textures owing to its superior stress homogenization and wear-debris management capabilities.

Based on the above analyses of the friction coefficient and potential, circular microtextures exhibit a stronger capability to maintain interfacial stability and passivation, and this superior performance is closely associated with their surface state. The two-dimensional wear-scar profiles and 3D morphologies shown in Fig. 13 further demonstrate that, from a macroscopic morphological perspective, the circular microtextured coating experienced the least material loss under corrosive wear conditions.

To verify this result and observe the macroscopic morphological characteristics of the worn surfaces, Figure 14 presents the SEM morphologies of the wear scars of the different coatings at 200 × magnification. Figure 14(a) shows the wear-scar morphology of the C coating, whose wear-scar width reached 504.6 μm, macroscopically confirming that it exhibited the greatest material loss. In contrast, the wear-scar widths of all textured coatings were significantly reduced. This phenomenon intuitively demonstrates that surface texturing can effectively distribute the contact load, thereby preventing large-area material spallation on the coating surface during friction. Macroscopically, the wear-scar width of $C_{C\text{-}T}$ was as low as 160.6 μm, in excellent correspondence with the shallowest wear depth shown in Fig. 14(c).

Macroscopic observation of the wear-scar morphology confirms that surface texturing effectively reduced coating wear. To further elucidate the underlying mechanism, this study conducted microscopic characterization of the wear-scar region of the untextured coating. Figure 15(b) shows that the wear scar of the untextured coating was wide with relatively well-defined edges. Figure 15(c) and (d) presents the secondary-electron and backscattered-electron morphologies of the wear-scar region at 5000 × magnification, further revealing the presence of numerous plowing grooves and lamellar spallation pits on the surface. This phenomenon indicates that, during the friction process, the wear mechanism was dominated by abrasive wear and fatigue spallation. The elemental analysis results for this region are summarized in Table 4. The elemental distribution within the wear-scar region was analyzed by EDS mapping, as shown on the right side of Fig. 15. The results indicate that Al, Co, and Cr were relatively uniformly distributed, whereas Fe and Ni exhibited pronounced localized depletion. Moreover, these depleted regions strongly coincided with the dark areas within the wear scar and the Cl- and Na-enriched zones. This phenomenon can be attributed to selective phase corrosion under the coupled action of wear and corrosion. In the dual-phase structure of the $AlCoCrFeNi_{2.1}$ eutectic high-entropy alloy, the Fe-Ni-rich FCC phase acts as the anodic phase and undergoes preferential dissolution, thereby initiating an autocatalytic corrosion cycle that promotes the enrichment of Cl^{-} and Na^{+} in the active regions. This phenomenon can be attributed to selective phase corrosion under the coupled effects of wear and corrosion. Meanwhile, oxygen was markedly enriched in the gray–white flat regions, indicating that a stable oxide layer formed in these areas during the wear process. Such heterogeneous elemental distribution reflects the occurrence of nonuniform oxidation in the coating under the combined action of wear and corrosion.

Figure 15 shows the wear-scar morphology of the circularly textured $AlCoCrFeNi_{2.1}$ eutectic high-entropy alloy coating after the tribocorrosion test. Compared with the other coatings, this coating exhibited markedly improved wear morphology, with only minor spalled layers and adhered debris observed, while typical severe wear features such as pronounced plowing grooves or lamellar spallation pits were absent. This indicates that its wear mechanism was predominantly characterized by mild adhesive wear. To further examine the surface micromorphology, high-magnification observations of the wear-scar region were conducted in secondary-electron (SE) and backscattered-electron (BSE) modes. The elemental composition of this region is presented in Table 5. The SE and BSE images reveal that the worn surface is generally flat and compact, with no microscopic cutting traces; only a small amount of adhesion-induced products are present, and no spallation caused by fatigue or brittle fracture is observed. These observations further confirm that the circular texture suppresses abrasive wear and fatigue spallation through uniform stress distribution and efficient wear-debris accommodation capacity.

Observe Fig. 16, EDS analysis of the wear-track surface indicates that the principal alloying elements, including Al, Co, Cr, Fe, and Ni, were homogeneously dispersed across the worn region, with no pronounced localized depletion of Fe and Ni as observed in the nontextured coating. Oxygen was distributed continuously and uniformly across the entire wear scar, indicating that a stable oxidation reaction occurred on the coating surface during the friction process, resulting in the in situ formation of a dense oxide layer. The oxide layer not only acts as a solid lubricant but also effectively prevents direct contact between corrosive species and the metallic substrate,

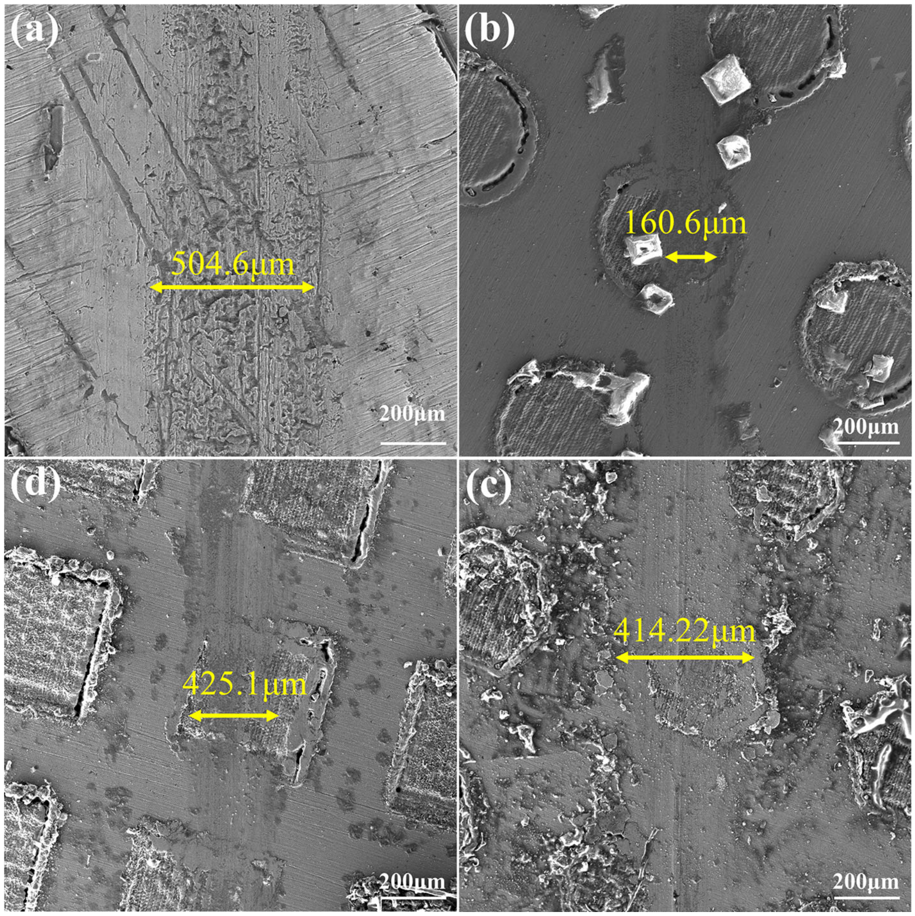

Fig. 14 Macroscopic morphologies after tribocorrosion: (a) SEM macroscopic morphology of the C coating after tribocorrosion; (b) SEM macroscopic morphology of C_{C-T} after tribocorrosion; (c) SEM macroscopic morphology of C_{S-T} after tribocorrosion; and (d) SEM macroscopic morphology of C_{H-T} after tribocorrosion

thereby suppressing the wear-accelerated corrosion effect and improving the tribocorrosion resistance of the coating.

The diagram in Fig. 17 schematically illustrates the rub abrasion characteristics of the coating after laser texturing. Laser-textured coatings exhibit an increased tendency to trap wear debris, thereby transforming harmful abrasive wear into beneficial adhesive wear and mitigating the direct wear of the coating, which ultimately leads to a significant improvement in tribological performance. Additionally, during the texturing process, the oxides generated on the surface provide an isolation layer to prevent direct contact between the metal substrate. The barrier bears the abrasion instead of the substrate material, thereby converting severe abrasive wear into mild oxidative wear. Following laser texturing, the grain refinement within the coating increases the number of grain boundaries, which impedes dislocation motion and microcrack propagation. This enhanced barrier effect increases the resistance of the material to plastic deformation and spallation, thereby increasing the surface strength and ultimately resulting in superior wear resistance. Compared with C_{S-T} and C_{H-T}, C_{C-T} more uniformly distributes stress, prevents stress concentration and crack initiation at sharp corners, provides more stable debris accommodation, and improves the coating performance. Compared with the C_{S-T} and C_{H-T} coatings, the C_{C-T} coating more uniformly distributes stress, prevents stress concentration and crack initiation at sharp corners, and provides more stable debris accommodation, thereby increasing the wear resistance of the coating.

Under secondary thermal input, the textured surface underwent thermal oxidation, resulting in the formation of circularly distributed oxides (shown in green in Fig. 17). These oxides possess high hardness, which helps reduce direct metal-to-metal contact during friction. Moreover, the textured dimples effectively trap and retain wear debris, preventing it from rolling repeatedly toward the interface and causing third-body abrasion.

4. Conclusion

In this study, three microtextures—circular, hexagonal, and square—were fabricated on an $AlCoCrFeNi_{2.1}$ coating to investigate the effect of texture morphology on surface performance. The main conclusions are as follows:

(1) During laser texturing, thermomechanical coupling significantly modified the surface. The high thermal input promoted surface oxidation, forming dense and well-adhered oxide layers in the textured regions, thereby improving wear resistance. Meanwhile, secondary laser heating refined the surface grains from coarse columnar grains of 300-450 μm in the bonding zone to ultrafine

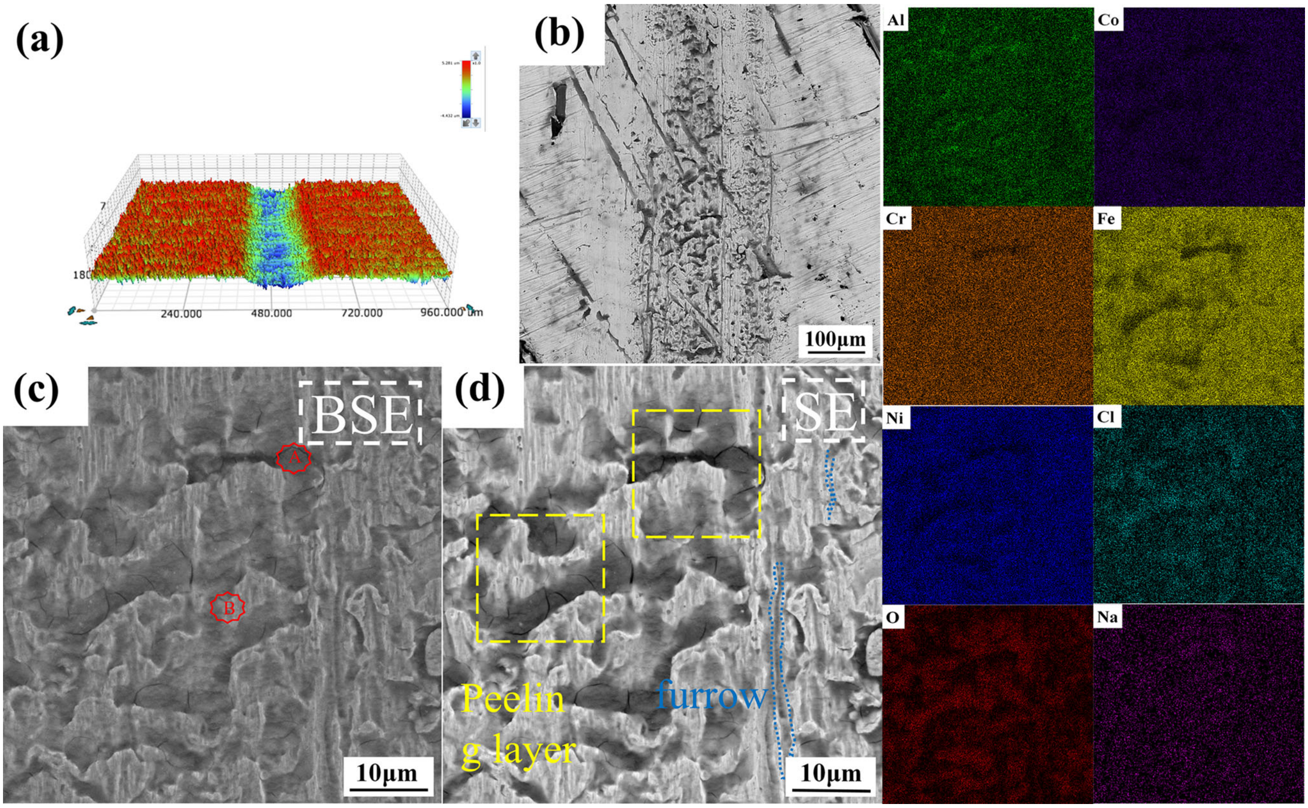

Fig. 15 Tribocorrosion wear track of C: (a) white-light morphology of the tribocorrosion wear track of C; (b) SEM macroscopic morphology of the tribocorrosion wear track of C; (c) SEM microscopic backscattered-electron morphology of the tribocorrosion wear track of C; and (d) SEM microscopic secondary-electron morphology of the tribocorrosion wear track of C and corresponding EDS analysis

Table 4 Point area energy spectrum analysis results

Ingredient, at.%								
Region	Al	Co	Cr	Fe	Ni	Cl	Na	O
A	4.47	9.47	12.03	34.48	18.55	2.25	1.85	16.91
B	4.60	10.19	11.48	35.17	19.92	1.42	1.53	14.69

Table 5 Point area energy spectrum analysis results

Ingredient, at.%								
Region	Al	Co	Cr	Fe	Ni	Cl	Na	O
A	39.20	4.55	5.13	13.72	7.73	0.45	0.44	28.77
B	4.18	6.60	11.3	22.78	25.78	4.16	0.58	20.69

equiaxed grains of 50-150 μm in the surface layer. The increased KAM value indicated higher dislocation density, contributing to surface strengthening.

(2) Compared with the nontextured coating, all laser-textured coatings exhibited improved tribological performance. Grain refinement, dislocation strengthening, debris trapping by textured dimples, and the protective oxide layer jointly reduced friction and wear. Among them, CC-T showed the best overall performance due to its superior debris-trapping ability and isotropic geometry, which promoted uniform stress distribution, delayed crack initiation, and enhanced coating reliability under sliding conditions.

(3) Surface texturing also improved the tribocorrosion resistance of the $AlCoCrFeNi_{2.1}$ coating in NaCl solution, with CC-T again exhibiting the best performance. The circular texture reduced stress concentration, retained wear debris, and promoted stable dynamic repassivation. As a result, CC-T showed the most stable friction response, shallowest wear track, and narrowest wear scar, while suppressing abrasive wear, fatigue spallation, and selective Fe-Ni dissolution.

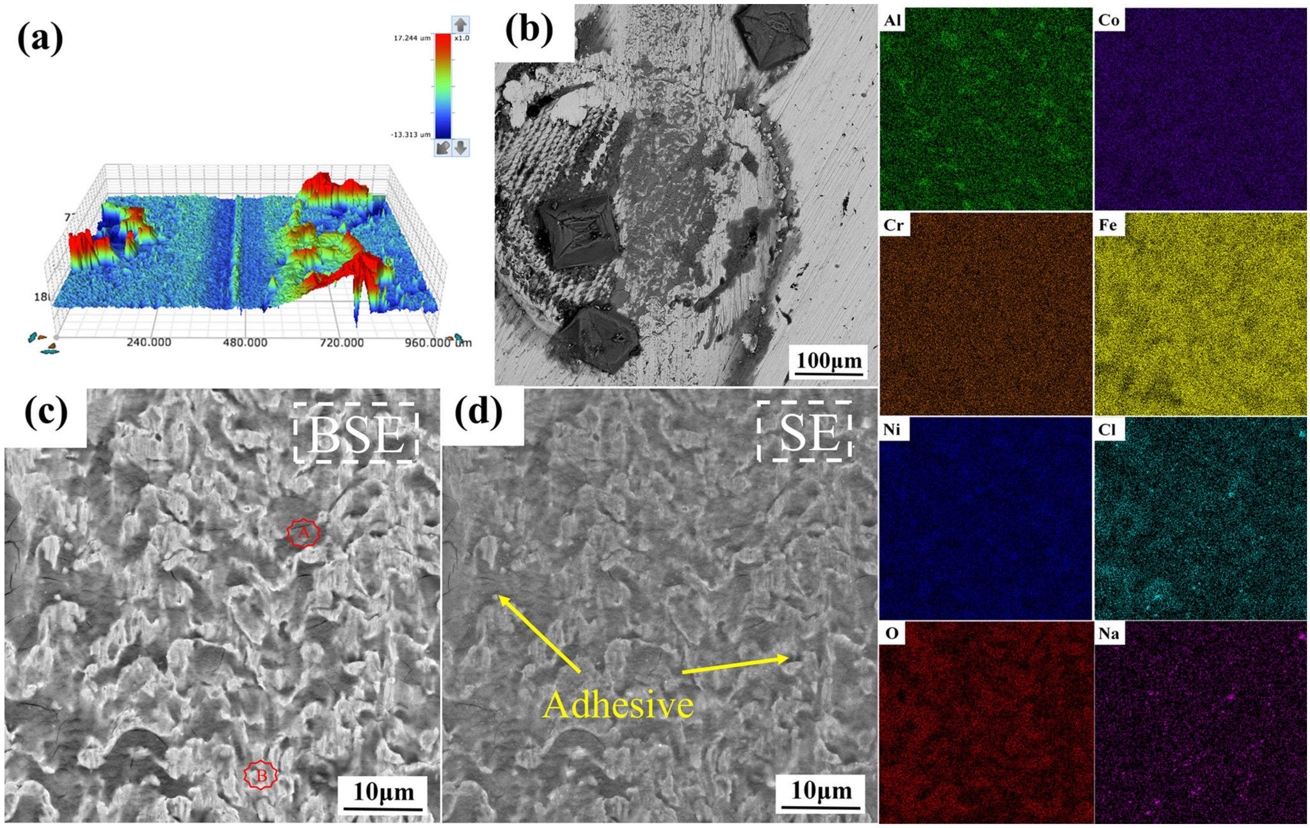

Fig. 16 Tribocorrosion wear track of the $C_{C\text{-}T}$ coating: (a) white-light morphology of the tribocorrosion wear track of $C_{C\text{-}T}$; (b) SEM macroscopic morphology of the tribocorrosion wear track of $C_{C\text{-}T}$; (c) SEM microscopic backscattered-electron morphology of the tribocorrosion wear track of $C_{C\text{-}T}$; and (d) SEM microscopic secondary-electron morphology of the tribocorrosion wear track of $C_{C\text{-}T}$ and corresponding EDS analysis

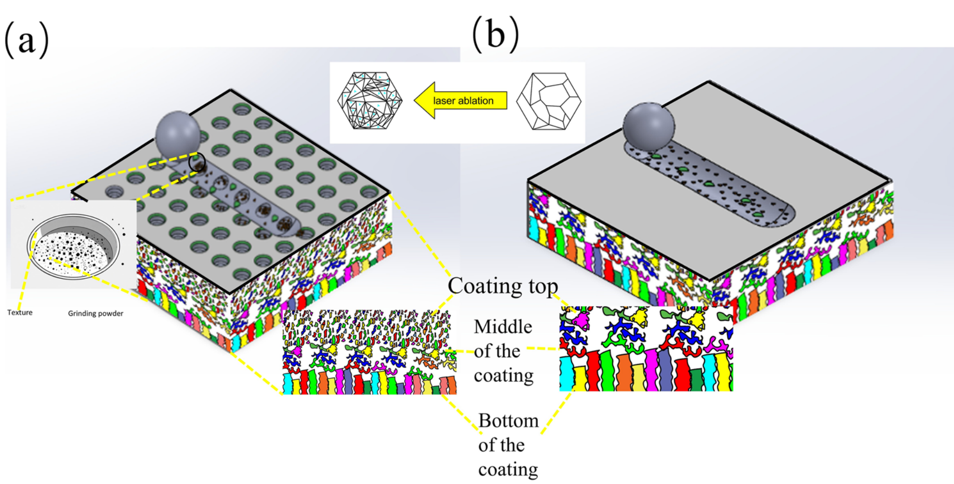

Fig. 17 Schematic diagram of the wear mechanism for the textured coatings: (a) after laser texturing and (b) before laser texturing

Acknowledgments

The paper was financially supported by National Natural Science Foundation of China (52405211), Tianjin Science and Technology Plan Project (25JCQNJC00520), Joint Fund of Henan Province Science and Technology R&D Program (Project NO. 245200810042), Guangdong Basic and Applied Basic Research Foundation (Grant No. 2023A1515240084), Guangdong Provincial University Key Research Project (Approval No. 2024ZDZX3014), and Tianjin Science and Technology Plan Project 24PTLYHZ00030.

Author Contributions

Xina Wang was involved in methodology, validation, writing—original draft, and writing—review and editing. Na Tan took part in resources, writing—original draft, supervision, and writing—review. Changqing Ye was responsible for methodology and resources. Yang Li contributed to writing—original draft, resources, supervision, and writing—review. Shulong Ye participated in formal analysis. Jingyi Tan participated in data collection. Yongjuan Dai reviewed. Yang Ding provided critical.

Data Availability

Data will be made available on request.

Conflict of interest

The authors declare that they have no known competing financial interests or personal relationships that could have appeared to influence the work reported in this paper.

References

1. Z.Y. Hu, L. Hua, Z.Y. Mei, L.G. Peng, S.S. Min, and W. Liu, corrosion Fatigue Life Prediction Model for 10CrNiCu Shipbuilding Steel under Authentic Marine Environments, *Case Stud. Constr. Mater.*, 2024, **1**(21), p e03787.
2. C.Y. Yang, R. Deng, R.Z. Wei, H. Li, R. Wang, and C.J. Zhao, Methods and Techniques for Enhancing Wear Resistance of Laser Cladding Coatings: A Comprehensive Review, *J. Manuf. Process.*, 2025, **152**, p 1123–1149.
3. Y.Y. Jiang, Z. Wen, Y.X. Chen, C. Xiang, and S.Q. Chao, Friction and Wear Failure Mechanism Analysis of QT600-3 Ductile Iron Elevator Traction Sheave, *Eng. Fail. Anal.*, 2025, **173**, p 109414.
4. W. Wang, J. Chen, K. He, X.Y. Cao, X.F. Gong, C.M. Tang, and Z.B. Cai, Water Droplet Erosion Behavior of Physical Vapor Deposition Deposited TiN, CrN and Multilayer Ti/TiAlN Coatings: A Comparative Study, *Thin Solid Films*, 2025, **825**, p 140742.
5. Y.L. Zha, Y.L. Su, Q.W. Huang, H.L. Fan, M. Guo, B.Y. Ha, and S.Y. Chen, Investigation on Tribological Properties of Plasma Sprayed FeCoNiCrAl High-Entropy Alloy Coatings under Different Sand Densities, *Colloid. Surface. A.*, 2025, **726**(3), p 137967.
6. Z.Y. Ren, Y.L. Hu, Y. Tong, Z.H. Cai, J. Liu, H.D. Wang, J.Z. Liao, S. Xu, and L.K. Li, Wear-Resistant NbMoTaWTi High Entropy Alloy Coating Prepared by Laser Cladding on TC4 Titanium Alloy, *Tribol. Int.*, 2023, **1**(182), p 108366.
7. K. Wen, G.W. Zhang, Z.C. Zhang, S. Xue, G.L Bai, Y.N. Han, and H. Xu, Enhanced Bonding Strength of Al/Fe Bimetal by Ni-Based Alloys Ni-Based Interlayer Prepared by Laser Cladding Technique, *Mater. Today. Commun.*, 2024, **38**, p 107906.
8. C.Y. Deng, W. Chen, and Y.X. Zhu, Experimental and Numerical Investigation of Bonding Strength in Laser Cladding: Fe-Based Cladding Layer with Varying WC Contents Coating on AISI H13 Substrate, *Opt. Laser Technol.*, 2025, **187**, p 112877.
9. J. Kim, G. Kim, C.H. Yim, J.E. Cho, N.K. Park, D.S. Yun, T.G. Lee, R.H. Chung, and D.G. Hong, Thermal-Profile Prediction of Heat-Affected Zone for Predictive Control during Laser Cladding, *Opt. Laser Technol.*, 2025, **1**(192), p 113903.
10. Z.T. Gao, T.X. Cheng, N.N. Zhang, Q.H. Bi, Z.M. Gao, C,W, Zhang, and Y. Yu Thermal-Mechanical Coupling Simulation and Experimental Study of Ultrasound-Assisted Laser Cladding of Ni60 Coating, *J. Alloy. Compd.*, 2025, **1024**, p 180270.
11. O. Devojno, E. Feldshtein, M. Kardapolava, and N. Lutsko, On the Formation Features, Microstructure and Microhardness of Single Laser Tracks Formed by Laser Cladding of a NiCrBSi Self-Fluxing Alloy, *Opt. Laser. Eng.*, 2018, **106**, p 32–38.
12. O. Conde, A.J. Silvestre, and J.C. Oliveira, Influence of Carbon Content on the Crystallographic Structure of Boron Carbide Films, *Surf. Coat. Tech.*, 2000, **125**(1–3), p 141–146.
13. L.J. Xu, S.Y. Sun, J.N. Xia, Z.H. Liu, W.J. Deng, J.X. Li, T. Wu, X.R. Zhu, Z.H. Lv, J.C. Gao, and J.K. Jiao, Effect of WC Content on Microstructure, Mechanical Properties, and Tribo-Corrosion Behavior of Laser-Cladded Ni40A/WC Composite Coatings on H13 Steel, *Mater Charact*, 2025, **224**, p 115072.
14. T.T. Jin, Y.S. Shi, J.W. Ding, Y. Wang, S.H. Hu, W. Zhang, and Y.B. Peng, Laser Cladding of Diamond Reinforced Composite Coatings on the Rotary Tiller Blade with Complex Curved Surface: Cladding Paths and Residual Stress, *Surf. Coat. Tech.*, 2025, **516**, p 13273.
15. X.D. Yang, W.G. Chen, D.Y. Li, Y. Zhang, Z.Y. Li, B.G. Dai, J.H. Zhang, and J.W. Yang, Research Progress on the Friction Reduction Characteristics of Surface Texturing Modifications Insliding Bearings, *Mater. Prot.*, 2024, **57**(7), p 154–164.
16. H. Jiang, J.Z. Hu, F.Y. Luo, Y. Zhao, and W.Q. Shi, Fe-Based Amorphous Reinforced CoCrFeNi HEA Composite Coating Prepared by Laser Cladding, *Mater. Res. Technol.*, 2024, **31**, p 1912–1923.
17. F. Song, X.F. Yang, W.L. Dong, Y.Q. Zhu, Z.Y. Wang, and M. Wu, Research and Prospect of Textured Sliding Bearing, *Nt. J. Adv.*, 2022, **121**, p 1–25.
18. S.L. Yuan, N.M. Zou, J.J. Liu, Z.Q. Wang, Z.X. Tian, L.H. Qin, L. Zhang, H.X. Wang, Z.H. Tang, B. Wu, and Y. Cheng, Effect of Laser Surface Texturing (LST) on Tribological Behavior of Double Glow Plasma Surface Zirconizing Coating on Ti6Al4V Alloy, *Surf. Coat. Tech.*, 2019, **368**, p 97–109.
19. Z.Q. Wang, R.H. Ye, and J.B. Xiang, The Performance of Textured Surface in Friction Reducing: A Review, *Tribol. Int.*, 2023, **177**, p 108010.
20. G.P. Lin, Z.B. Cai, B.W. Lu, L. Gu, Y.L. Wang, X.C. Yan, H. Qiu, J. Guo, Z. Dong, and F.H. Li, Enhanced Wear Resistance of Laser Cladded WC-Ni Composite Coatings by Picosecond Laser Surface Texturing, *Tribol. Int.*, 2025, **204**, p 110517.
21. M. Vishnoi, P. Kumar, and Q. Murtaza, Surface Texturing Techniques to Enhance Tribological Performance: A Review, *Surf. Interfaces.*, 2021, **27**, p 101463.
22. S. Yuan, N.M. Lin, J.J. Zou, Z.Q. Liu, Z. X.Wang, L.H. Tian, L. Qin, H.X. Zhang, Z.H. Wang, B. Tang, and Y.C. Wu, Effect of Laser Surface Texturing (LST) on Tribological Behavior of Double Glow Plasma Surface Zirconizing Coating On Ti6al4v Alloy, *Surf. Coat. Technol.*, 2019, **25**(368), p 97–109.
23. S. Yuan, N.M. Lin, W.H Wang, H.X. Zhang, Z.Q. Liu, Y. Yu, Q.F. Zeng, and Y.C. Wu, Correlation Between Surface Textural Parameter and Tribological Behaviour of Four Metal Materials with Laser Surface Texturing (LST), *Appl. Surf. Sci.*, 2022, **1**(583), p 152410.
24. X.Y. Chen, Y.L. Li, W.P. Rao, Y.R. Lin, J.Y. Chen, Q.S. Jiang, Z.L. Xu, B.C. Guo, J.S. Gao, and S. Huang, Study on Friction and Wear of 9Cr18 Steel with Composite Treatment of Laser Shock Processing and Surface Texturing, *J. Mater. Res. Technol.*, 2025, **37**, p 1119–1133.
25. X.D. Zhao, Y.M. Zhang, and S.Z. Gao, Analysis and Evaluation of the Synergistic Effect of Ceramic Materials and Surface Texture on Anti-abrasive Particle Wear under Rolling Conditions, *Tribol. Int.*, 2024, **197**, p 109821.
26. L.X. Chen, Y.Y. Zhu, H.H. Huang, D. Zhou, K.Y. Peng, and Y.S. Wang, Process-Surface Topography-Tribological Performance of Surface Micro-textures by Nanosecond Laser Ablation with Low-Melting Alloy Coatings, *Tribol. Int.*, 2026, **214**, p 111167.
27. C.Y. Hu, B. Han, M.Y. Li, X.D. Li, L.Q. Wang, C.L. Liu, Q. Zhang, T.G. Duan, J.Y. Song, and X.M. Wang, Effect of Micro-dimple Textures on the Tribological Performance of CoCrFeNiMoW High-Entropy Alloy, *Surf. Coat. Technol.*, 2025, **515**, p 132628.
28. X.D. Yang, W.G. Chen, Y. Zhang, B.G. Dai, Z.Y. Li, J.W. Yang, J.H. Zhang, D.Y. Li, and Z.L. Qiu, Influence of Triangular Texture Composite MAO Coating on the Tribological Properties of Aluminum Alloys, *Tribol. Int.*, 2025, **201**, p 110243.
29. J.L. Guo, C.D. Li, Q.D. Du, and Y.H. Liu, Tuning the Tribological Properties of Micro-arc Oxidation Coatings under Dry and Starved Lubrication Conditions via Laser Texturing and Surface Chemistry, *Ceram. Int.*, 2025, **51**, p 32919–32930.
30. X. Tong and X. Li, Study on Noise Behavior of Micro-textured Composite Coated Cemented Carbide Surface Grinding Titanium Alloy Based on HHT Analysis, *J. Vib. Control*, 2024, **30**, p 3472–3488.
31. Y. Fu, J. Li, H. Luo, C.W. Du, and X.G. Li, Recent Advances on Environmental Corrosion Behavior and Mechanism of High-Entropy Alloys, *J. Mater. Sci. Technol.*, 2021, **80**, p 217–233.
32. Y.F. Yang, F. Hu, T. Xia, R.H. Li, J.Y. Bai, J.Q. Zhu, J.Y. Xu, and G.F. Zhang, High Entropy Alloys: A Review of Preparation Techniques, Properties and Industry Applications, *J. Alloy. Compd.*, 2025, **1010**, p 177691.

33. T. Hu, L.X. Xie, J.W. Chen, Z.Y. Huang, and J.X. Wang, Numerical Study on Tribology Properties of Textured Surfaces Based on a New Contact Model, *Mater. Today. Commun.*, 2024, **40**, p 109969.
34. Z.W. Wang, W.C. Liu, W. Yuan, J.C. Cong, P. Chander, L.Y. Wu, and H.Y. Zheng, The Effect of Laser In-Situ Induced Graphene-Like Micro-texture on the Friction and Wear Properties of Ductile Cast Iron, *J. Mater. Res. Technol.*, 2021, **1**(12), p 2407–2413.
35. B. Cantor, Multicomponent High-Entropy Cantor Alloys, *Prog. Mater. Sci.*, 2021, **120**, p 100754.
36. R. Neuvonen, T. Skriko, and T. Bjrk, Discretization and Material Parameter Characterization for a HAZ in Direct-Quenched Armor Steel, *Eur. J. Mech. A-Solid.*, 2021, **89**, p 104305.
37. B. Han, S.Y. Zhang, T.M. Zhang, Y.H. Chen, X.W. Qin, M.Y. Li, C.Y. Hu, M.W. Wei, and X.X. Xue, Hardness Enhancement Mechanism of AlxCoCrFeNiSi High-Entropy Alloy Coatings Prepared by Laser Cladding, *Intermetallics*, 2023, **158**, p 107909.
38. W. Wang, T. Lyu, H.S. Choi, C. Cheng, and Y. Zou, Wear Mechanism Transitions in FeCoNi and CrCoNi Medium-Entropy Alloys from Room Temperature to 1,000 °C, *J. Mater. Sci. Technol.*, 2025, **231**, p 151–163.
39. Z. Li, L. Wang, Y. Yang, C. Liu, B.X. Su, Q.D. Zhang, Z.W. Li, J.Q. Huang, B.B. Wang, L.S. Luo, R.R. Chen, and Y.Q. Su, High Temperature Oxidation Behavior of TiNbMoAlSi Refractory High Entropy Alloy Developed by Electron Beam Additive Manufacturing, *J. Mater. Sci. Technol.*, 2025, **215**, p 131–146.
40. Y. Xing, C.J. Li, Y.K. Mu, Y.D. Jia, K.K. Song, J. Tan, G. Wang, Z.Q. Zhang, J.H. Yi, and J. Eckert, Strengthening and Deformation Mechanism of High-Strength CrMnFeCoNi High Entropy Alloy Prepared by Powder Metallurgy, *J. Mater. Sci. Technol.*, 2023, **132**, p 119–131.
41. K. Sikdar, A. Bhattacharya, C. Chottopadhyay, D. Roy, and R. Mitra, An Insight into High Temperature Stability of Microstructure and Mechanical Properties of Bulk Nanocrystalline $(AlCoCrCuFeNi)_{99}B1$ High Entropy Alloy Processed by Mechanical Alloying and Spark Plasma Sintering, *Mater. Sci. Eng. A*, 2025, **936**, p 148408.
42. Y.K. Zhou, J.J Kang, G.Z. Ma, L.N. Zhu, Q. Da, B. Liu, R.F. Li, Microstructure, mechanical and wear behavior of $Al_xTi_{(1-x)}CoCrFeNi$ (x = 0.875, 0.75) high-entropy coatings fabricated via HVOF and post-annealing. *Tribol. Int.* 2025, **201**, 110248
43. J.L. Wang, B. Han, Z.B. Chen, C.Y. Hu, Q. Zhang, and C. Wang, Study on Tribological Oxide Mechanism of CoCrFeNiMo High Entropy Alloy, *Wear*, 2023, **526–527**, p 204907.
44. K.X. Xu, M. Zhu, Y.F. Yuan, and S.Y. Guo, The Corrosion Behavior and Mechanism of CoCrFeNi High-Entropy Alloy Subjected to AC Interference in a Simulated Littoral Environment, *J. Mater. Eng. Perform.*, 2025, **34**(11), p 9412–9427.
45. C.X. Han, Y. Zhang, J.S. Liu, Z. Li, Y.N. Wu, Y.Q. Cui, F. Wang, and Z.T. Liu, Effect of Mo Content on Microstructure and Mechanical Properties of CoCrFeNi Series High-Entropy Alloys, *J. Mater. Res. Technol.*, 2024, **30**, p 8209–8217.
46. Y. Wang, G.L. Li, H. Qi, W. Zhang, R.R. Chen, R.M. Su, and Y.D. Qu, Effect of Al Content on the Corrosion Behavior and Mechanism of $Al_xCoCrFeNi$ High-Entropy Alloys, *J. Mater. Res. Technol.*, 2025, **51**(30), p 32919–32930.
47. T.X. Bui, T.H. Fang, and C.I. Lee, Deformation and Machining Mechanism of Nanocrystalline NiCoCrFe High Entropy Alloys, *J. Alloy. Compd.*, 2022, **924**, p 166525.
48. X.Z. Chen, C.Y. Wu, Y.M. Rong, G.J. Zhang, and Y. Huang, Preparation of a Super Wear-Resistant Surface on WC-Co Cemented Carbide by Combing Femtosecond Laser Texturing and DLC Coating, *Ceram. Int.*, 2025, **51**(29), p 59996–60009.
49. X. Zhang, J.H. Li, and H.H. Yang, Interfacial Tribological Behavior and Wear Resistance Mechanisms in TiAlN-Coated Bionic Micro-textured Surfaces, *Mater. Chem. Phys.*, 2026, **347**, p 131490.
50. Y.D. Yan, L.T. Mu, Y. Liu, Q. Li, Y. Liu, Z. Ma, J.W. Xu, and K.X. Di, Enhanced Wear Resistance, Corrosion Resistance and Biocompatibility on Micro-texture Ti6Al4V Surfaces by Pulse Laser Remelted, *Surf Coat Tech.*, 2025, **513**, p 132528.
51. X.Y. Chen, Y.L. Li, W.P. Rao, Y.R Lin, J.Y. Chen, Q.S. Jiang, Z.L. Xu, B.C. Guo, J.S Gao, and S. Huang, Study on Friction and Wear of 9Cr18 Steel with Composite Treatment of Laser Shock Processing and Surface Texturing, *J. Mater. Res. Technol.*, 2025, **1**(37), p 1119–1133.
52. M.A. Teplonogova, K.A. Emelyanenko, A.M. Emelyanenko, and L.B. Boinovich, Balancing Heat and Pulse Width in Laser Texturing of Al-Mg alloy: Super Hydrophobicity with Wear, Icing, and Corrosion Control, *Surf Coat Tech.*, 2025, **518**, p 132876.
53. P. Han, S.C. Yang, and Z.K. Ren, Research on Micro-texture and Coating Preparation Process Strategy for Macro and Micro Properties of Cemented Carbide Surface, *Int J Refract Met H.*, 2026, **135**, p 107503.
54. L.W. Guo, Q.D. Li, W.H. Guo, H.W. Hu, J. Dai, N. Rong, B. Long, X.F. Gong, and H.M. Meng, Electrochemical Corrosion Behavior of ICr12Ni3Mo2VN Stainless Steel, *Mater. Prot.*, 2024, **57**(8), p 105–114.
55. Y.K. Lan, W.M. Guo, S.B. Yu, H.H. Zheng, Y.X. Zhang, X.F. Wang, S. Zhao, G.Z. Liu, J.F. Zhang, and B. Liu, High-Temperature Wear Behavior of Precipitation-Strengthened High-Entropy Alloy Composite Coatings Developed by Laser Cladding Technology, *Tribol. Int.*, 2026, **216**, p 111553.
56. T.L. Schmitz, J.E. Action, D.L. Burris, J.C. Ziegert, and W.G. Sawyer, Wear-Rate Uncertainty Analysis, *J. Tribol.*, 2004, **126**(4), p 802–808.
57. Z.Z. Chong, Y.N. Sun, W.J. Cheng, L.F. Huang, C.Y. Han, X.F. Ma, and A.C. Meng, Laser Remelting Induces Grain Refinement and Properties Enhancement in High-Speed Laser Cladding AlCoCrFeNi High-Entropy Alloy Coatings, *Intermetallics*, 2022, **150**, p 107686.
58. Y. Guo, H. Su, Z. Shen, H. Gao, P. Yang, X. Li, C. Huo, Q. Hu, and X. Li, Rapid Solidification Microstructure Evolution Behavior of AlCoCrFeNi2.1 Eutectic High-Entropy Alloys Fabricated by Laser Powder-Bed Fusion, *J. Mater. Sci. Technol.*, 2026, **262**, p 1–12.
59. W.L. Hsu, C.W. Tsai, A.C. Yeh, and J.W. Yeh, Clarifying the Four Core Effects of High-Entropy Materials, *Nat. Rev. Chem.*, 2024, **8**, p 471–485.
60. L. Zhang, Y. Ji, Y.X. Wang, and B. Yang, Enhanced Hot Corrosion Resistance of AlCoCrFeNi2.1 High Entropy Alloy Coatings by Extreme High-Speed Laser Cladding, *Corros. Sci.*, 2024, **240**, p 112486.

Publisher's Note Springer Nature remains neutral with regard to jurisdictional claims in published maps and institutional affiliations.